

EDGE: the puzzling ellipticity of Eridanus II's star cluster and its implications for dark matter at the heart of an ultra-faint dwarf

Matthew D. A. Orkney [®], ^{1,2}★ Justin I. Read [®], ¹ Oscar Agertz [®], ³ Andrew Pontzen, ⁴ Martin P. Rey [®], ^{3,5} Alex Goater, ¹ Ethan Taylor, ¹ Stacy Y. Kim¹ and Maxime Delorme ⁶

Accepted 2022 June 20. Received 2022 June 11; in original form 2022 January 30

ABSTRACT

The Eridanus II (EriII) 'ultra-faint' dwarf has a large (15 pc) and low-mass $(4.3 \times 10^3 \, \rm M_\odot)$ star cluster (SC) offset from its centre by 23 ± 3 pc in projection. Its size and offset are naturally explained if EriII has a central dark matter core, but such a core may be challenging to explain in a Λ CDM cosmology. In this paper, we revisit the survival and evolution of EriII's SC, focusing for the first time on its puzzlingly large ellipticity $(0.31^{+0.05}_{-0.06})$. We perform a suite of 960 direct *N*-body simulations of SCs, orbiting within a range of spherical background potentials fit to ultra-faint dwarf (UFD) galaxy simulations. We find only two scenarios that come close to explaining EriII's SC. In the first scenario, EriII has a low-density dark matter core (of size \sim 70 pc and density $\lesssim 2 \times 10^8 \, \rm M_\odot \, kpc^{-3}$). In this model, the high ellipticity of EriII's SC is set at birth, with the lack of tidal forces in the core allowing its ellipticity to remain frozen for long times. In the second scenario, EriII's SC orbits in a partial core, with its high ellipticity owing to its imminent tidal destruction. However, this latter model struggles to reproduce the large size of EriII's SC, and it predicts substantial tidal tails around EriII's SC that should have already been seen in the data. This leads us to favour the cored model. We discuss potential caveats to these findings, and the implications of the cored model for galaxy formation and the nature of dark matter.

Key words: methods: numerical – galaxies: dwarf – galaxies: haloes – galaxies: individual: Eridanus II – galaxies: star clusters: general – galaxies: structure.

1 INTRODUCTION

The standard cosmological model (ACDM) provides an excellent match to the observed growth of cosmic structure on large scales (e.g. Clowe et al. 2006; Springel, Frenk & White 2006; Tegmark et al. 2006; Dawson et al. 2013; Oka et al. 2014; Planck Collaboration XVI 2014; Wang et al. 2016). However, pure dark matter structure formation simulations in a ACDM cosmology deviate from observations on galactic and sub-galactic scales, where 'baryonic physics' - e.g. gas cooling, star formation, 'feedback' from massive stars becomes important (Carignan & Freeman 1988; Flores & Primack 1994; Moore 1994; Klypin et al. 1999; Moore et al. 1999; McGaugh, Rubin & de Blok 2001; Sand, Treu & Ellis 2002; Okamoto & Frenk 2009; Boylan-Kolchin, Bullock & Kaplinghat 2011). The earliest such tension has become known as the 'cusp-core problem', and concerns the central densities of dark matter haloes in dwarf galaxies. Pure dark matter simulations in a ACDM cosmology predict the formation of a complex web of cosmic structure punctuated by dense

Analysis of real galaxies reveals a more complicated picture. Many dwarf galaxies favour a flatter central density than predicted by the NFW profile (Carignan & Freeman 1988; Flores & Primack 1994; Moore 1994; McGaugh et al. 2001; Read et al. 2017a), while others are consistent with a dense NFW cusp (Richardson & Fairbairn 2014; Strigari, Frenk & White 2017; Read, Walker & Steger 2018; Shi et al. 2021). Recently, Read, Walker & Steger (2019) found that the densest dwarfs appear to be those with the least star formation, while the dwarfs with lower central densities have experienced more star formation. This is exactly what was predicted by models in which

¹Department of Physics, University of Surrey, Guildford, GU2 7XH, United Kingdom

²Institut de Ciènces del Cosmos (ICCUB), Universitat de Barcelona (IEEC-UB), Martí i Franquès 1, E-08028 Barcelona, Spain

³Lund Observatory, Department of Astronomy and Theoretical Physics, Lund University, Box 43, SE-221 00 Lund, Sweden

⁴Department of Physics and Astronomy, University College London, London WC1E 6BT, UK

⁵Sub-department of Astrophysics, University of Oxford, DWB, Keble Road, Oxford OX1 3RH, UK

⁶Département d'Astrophysique/AIM, CEA/IRFU, CNRS/INSU, Université Paris-Saclay, F-91191 Gif-Sur-Yvette, France

haloes that have a self-similar density profile (Navarro, Frenk & White 1997). These density profiles are well fitted within an accuracy of $\sim \! 10$ per cent by the 'NFW' profile (Navarro, Frenk & White 1996b), which is described by a divergent inner density that goes as $\rho \propto r^{-1}$ and outer density that goes as $\rho \propto r^{-3}$.

 $^{^1\}mathrm{This}$ self-similarity is predicted to end at around an Earth-mass for a $\sim\!100\,\mathrm{GeV/c^2}$ weakly interacting massive particle due to the free-streaming limit (Hofmann, Schwarz & Stöcker 2001; Diemand, Moore & Stadel 2005; Wang et al. 2020b). This is currently far below the resolution limit of most cosmological simulations.

^{*} E-mail: m.d.a.orkney@gmail.com

dark matter cusps are transformed to lower density cores by repeated stellar-feedback-induced gravitational potential fluctuations (e.g. Navarro, Eke & Frenk 1996a; Read & Gilmore 2005; Mashchenko, Couchman & Wadsley 2006; Mashchenko, Wadsley & Couchman 2008; Pontzen & Governato 2012; Di Cintio et al. 2014). Further dynamical evidence for dark matter cusp-core transformations in galaxies at higher redshift has been recently reported by Genzel et al. (2020), Bouché et al. (2022), and Sharma, Salucci & van de Ven (2022).

While gas cooling and stellar feedback can transform dark matter cusps to cores, it is energetically challenging for this process to create large dark matter cores (typically > 500 pc) in the very smallest 'ultrafaint' dwarfs, since they form so few stars ($M_* < 10^5 \,\mathrm{M}_{\odot}$; Peñarrubia et al. 2012; Garrison-Kimmel et al. 2013; Di Cintio et al. 2014; Maxwell, Wadsley & Couchman 2015; Oñorbe et al. 2015; Tollet et al. 2016). However, smaller dark matter cores may still form inside the half-light radius ($R_{1/2} \sim 20-200 \,\mathrm{pc}$ for UFDs²), where the gravitational potential fluctuations are strongest (e.g. Oñorbe et al. 2015; Read et al. 2016). Whether this is expected to happen in a ACDM cosmology remains an active area of debate. Most studies to date find that cusp-core transformations are challenging at the likely mass-scale of UFDs $(M_{200c} \sim 10^9 \,\mathrm{M_\odot}; M_* \sim 10^5 \,\mathrm{M_\odot};$ e.g. Chan et al. 2015; Wheeler et al. 2019a; Gutcke et al. 2022). However, there are some notable exceptions. In recent work, Orkney et al. (2021) studied cusp-core transformations for UFDs drawn from the 'Engineering Dwarfs at Galaxy formation's Edge' (EDGE) simulation project (with a mass, baryonic mass, and spatial resolution of $120 \,\mathrm{M}_{\odot}$, $20 \,\mathrm{M}_{\odot}$, and 3 pc, respectively, sufficient to resolve dark matter cores in UFDs larger than ~ 20 pc). They found that UFDs can lower their inner dark matter density by up to a factor ~ 2 through a combination of early heating due to star formation, followed by late-time heating from minor mergers. While none of their simulated dwarfs formed a completely flat central core, their small sample size left open the possibility that this combination of mechanisms could form flatter cores for some rarer assembly histories. It is also important to note that dark matter core formation on these mass scales is very sensitive to small changes in the star formation and feedback modelling. Pontzen et al. (2021) showed that a small increase in variability of the star formation rate on time-scales shorter than the local dynamical time is sufficient to form a full dark matter core in an ultra-faint, without significantly altering its stellar mass. As such, the question of whether complete dark matter core formation is expected in some or all UFDs in ΛCDM remains open.

On the observational side, there is growing, albeit indirect, evidence for small dark matter cores in at least some UFDs (e.g. Amorisco 2017; Sanders, Evans & Dehnen 2018; Malhan, Valluri & Freese 2021), with the most compelling case being EriII (Amorisco 2017; Contenta et al. 2018). Discovered by the dark energy survey (DES, Bechtol et al. 2015; Koposov et al. 2015), EriII is an UFD with a stellar mass of $8.3^{+1.7}_{-1.4} \times 10^4 \, \mathrm{M}_\odot$ and a dynamical mass estimate of $1.2^{+0.4}_{-0.3} \times 10^7 \, \mathrm{M}_\odot$ within its half-light radius (Li et al. 2017). Its low metallicity implies an old stellar population and it is a good candidate for being a 'fossil' galaxy that was quenched by reionization (Simon et al. 2021). Deep imaging of EriII has revealed a lone SC offset in projection from EriII's photometric centre (Koposov et al. 2015; Crnojević et al. 2016; Simon et al. 2021), making it the faintest

known galaxy to host a SC. The large projected half-light radius of this SC (15 \pm 1 pc), and its large offset from EriII's photometric centre (23 \pm 3 pc; Simon et al. 2021³), can be naturally explained if it is orbiting within a central dark matter core of size $\sim\!70\,\mathrm{pc}$ and density $\lesssim\!2\times10^8\,\mathrm{M}_\odot\,\mathrm{kpc}^{-3}$ (Amorisco 2017; Contenta et al. 2018). By contrast, a 'pristine cuspy' inner dark matter profile – as expected in pure dark matter structure formation simulations in $\Lambda\mathrm{CDM}$ – rapidly destroys the SC, making such a scenario unlikely.

More recently, kinematic analysis of spectroscopic observations from the MUSE-faint survey has confirmed that the SC in EriII is indeed a self-bound object and is within the host galaxy (Zoutendijk et al. 2020). Expanding on this work, Zoutendijk et al. (2021b) use mass-modelling techniques on 92 tracer stars to show that a solitonic core dark matter model provides the best match for the potential profile of EriII (but that alternative DM models cannot be ruled out). This, then, can be considered direct and independent evidence favouring a core in EriII, which serendipitously supports a core radius in excess of the projected orbital offset observed for the SC (> 47 pc at 68 per cent confidence level).

In this paper, we revisit the survival and evolution of EriII's SCs, focusing for the first time on its puzzlingly large ellipticity $(0.31^{+0.05}_{-0.06},$ Simon et al. 2021). The ellipticity is a key new piece of information because, at first sight, it appears to pose an immediate problem for models in which the SC orbits within a constant density core. This is because: (i) the SC's short relaxation time ($t_{\rm relax} \sim 2 \, {\rm Gyrs}$; Contenta et al. 2018) should rapidly erase any birth ellipticity through two-body effects (e.g. Agekian 1958; Shapiro & Marchant 1976; Longaretti & Lagoute 1996; Einsel & Spurzem 1999a; Bianchini et al. 2013), and (ii) it is challenging to induce a high ellipticity with tides, since tidal forces formally vanish inside a constant density core⁴ (e.g. Contenta et al. 2018). As such, we set out in this paper to answer the question: can we form a SC as large, offset, and elliptical as that in EriII within realistic UFDs in \(\Lambda CDM? \) To address this question, we first select a number of 'ultra-faint' dwarfs from the EDGE simulation project (Rey et al. 2019; Agertz et al. 2020; Rey et al. 2020; Orkney et al. 2021; Pontzen et al. 2021, 2022; Rey et al. 2022), chosen to be most similar to EriII. We then set up a suite of 960 collisional NBODY6DF follow-up simulations that model SCs orbiting within spherically symmetric potentials fit to these dwarfs, sampling over a grid of initial properties and orbits. We consider a static pristine cold dark matter cusp, a static weakened cusp, a static partial dark matter core, and a mildly time-evolving partial core, each fit to a representative UFD drawn from the EDGE simulation suite. We also include, for comparison, the lower density cored potential from Contenta et al. (2018). This is more cored than any of the EDGE dwarfs presented in Orkney et al. (2021), but has properties similar to the cored UFD presented and discussed in Pontzen et al. (2021). We discuss whether such a cored model is likely in a ACDM cosmology in Section 4.

This paper is organized as follows. In Section 2, we describe the EDGE simulations used in this paper, and the motivation and setup for our collisional *N*-body simulation suite. We discuss the results of our cosmological simulations in Section 3.1, and present

²Whilst such cores would be small, they are none the less dynamically important by construction, since $R_{1/2}$ is the scale on which we can probe the inner gravitational potential of dwarfs via their stellar kinematics (Read, Agertz & Collins 2016).

³See also Martínez-Vázquez et al. (2021) who find an even larger offset and half-light radius, and a larger ellipticity.

⁴The tidal radius of a point mass SC of mass M_{SC} moving on a radial orbit in a power law background potential, $\rho \propto r^{-\gamma}$, is given by (e.g. Read et al. 2006a): $\frac{r_{\rm t}}{r_{\rm B}} \simeq \left[\frac{M_{\rm SC}}{M_{\rm B}(1-\gamma)}\right]^{1/3}$, where $M_{\rm B}$ is the background mass enclosed within $r_{\rm B}$ (valid for $\gamma < 1$). Thus, for a constant density core, $\gamma = 0$, $r_{\rm t} \simeq r_{\rm B}$, and inside the core $(r < r_{\rm B})$ there will formally be no tidal stripping.

the results for our *N*-body simulation suite in Section 3.2. Our discussion is presented in Section 4. In Section 4.1, we examine the core formation mechanisms in our EDGE simulations and consider whether alternative star formation and feedback physics, or alternative cosmologies could provide larger cores. In Section 4.2 and Section 4.3, we discuss possible pathways for the formation, evolution, and survival of the SC in EriII. Finally, in Section 5 we present our conclusions.

2 METHOD

2.1 Cosmological simulations of ultra-faint dwarfs

We analyse a selection of UFD galaxy simulations taken from the wider suite of cosmological zoom-in simulations that form the EDGE project (debuted in Agertz et al. 2020), modelled using the adaptive mesh refinement (AMR) tool RAMSES (Teyssier 2002). Our cosmological parameters are based on data from the Planck satellite (Planck Collaboration XVI 2014), and are $\Omega_{\rm m}=0.309$, $\Omega_{\Lambda}=0.691$, $\Omega_{\rm b}=0.045$, and $H_0=67.77$ km s⁻¹ Mpc⁻¹. Our baryonic physics recipe, zoom-halo selection criteria, and our simulation methods are all described in detail in Agertz et al. (2020). For completeness, we briefly summarize them here.

The fiducial baryonic physics model includes Schmidt-law star formation (Schmidt 1959), stellar evolution and stellar feedback budgets adopted from Agertz et al. (2013). Our feedback scheme models the injection of energy, momentum, and metals from supernovae (SNe) into the interstellar medium. A time-dependent, uniform ultraviolet background is used to model the epoch of reionization (based on Haardt & Madau 1996 with modifications as described in Rey et al. 2020). The hydrodynamic grid spatial resolution approaches $\sim\!3$ pc and $\sim\!20\,M_\odot$ within the zoom region, allowing us to resolve the impact of individual SNe on the intergalactic medium (Kimm et al. 2015; Wheeler et al. 2019b; Agertz et al. 2020).

All simulations are initialized with the GENETIC code (Stopyra et al. 2021) which allows us to forensically explore the impact of assembly history on galaxy properties using the genetic modification (GM) approach (Roth, Pontzen & Peiris 2016; Rey & Pontzen 2018). This involves altering the initial conditions of a cosmological simulation in a way that maximizes the chance that those alterations arise from a random Gaussian draw from a ΛCDM cosmology.

Detailed analysis was performed using the TANGOS data base package (Pontzen & Tremmel 2018) and the PYNBODY analysis package (Pontzen et al. 2013). We analyse four haloes previously described in Rey et al. (2019) and Orkney et al. (2021), all of which have a final stellar mass of $\mathcal{O}(10^5)\,M_\odot$ and are selected from the EDGE suite to be most similar to the observed properties of EriII (see Table 1). Halo1459 GM:Later and Halo1459 GM:Latest are based upon the initial conditions of Halo1459, but have been modified with our GM treatment. Halo1459 GM:Later (Halo1459 GM:Latest) has had its formation delayed such that it is a third (a half) times less massive than Halo1459 at the time of reionization.

We find that bound ensembles of stellar particles, which we tentatively identify as SCs, form naturally within all of our EDGE simulations. We will investigate the formation physics and properties of these SCs in forthcoming work (Taylor et al. 2022 in prep.). Here, we note that the long-term dynamical evolution of these SCs cannot be relied upon because the stars are not individually resolved, and the intra-particle forces are artificially damped by the \sim 3 pc force-softening. Therefore, SCs that develop in EDGE (and other similar cosmological simulations) are prone to artificial dissolution. Furthermore, our small sample of SCs in EDGE is not sufficient

For the simulated dwarfs, the velocity dispersion and uncertainty are determined using a bootstrapping technique with **Table 1.** Comparison between the properties of Erill and those of our simulated galaxies at z = 0. From left to right are the galaxy name, the virial mass, the total stellar mass, the projected half-light radius, EriII are gathered from the literature: a) Zoutendijk et al. 2021a (their 'core + tides' time, measured as the time when the main progenitor reaches 50 per cent of its final M_{200c} . the stellar metallicity

Name	$M_{200c}~[{ m M}_{\odot}]$	$M_* [{ m M}_\odot]$	R _{1/2} [kpc]	[Fe/H]	$\sigma_{\rm LOS} [{\rm km s^{-1}}]$	$ ho(40\mathrm{pc})[\mathrm{M}_\odot/\mathrm{kpc}^3]$	$M(< R_{1/2}) [{ m M}_{\odot}]$	t _{form} [Gyr]
Halo1445	1.32×10^{9}	1.35×10^{5}	0.10	-2.41	5.11 ± 0.51	4.78×10^{8}	9.93×10^{5}	3.79
Halo1459	1.43×10^{9}	3.77×10^{5}	0.10	-1.96	5.81 ± 0.53	6.89×10^{8}	1.91×10^{6}	2.83
Halo1459 GM:Later	1.43×10^{9}	1.11×10^{5}	0.20	-2.47	5.88 ± 0.57	3.43×10^{8}	2.92×10^{6}	3.19
Halo1459 GM:Latest	1.38×10^{9}	8.65×10^{4}	0.30	-2.80	6.12 ± 0.48	3.62×10^{8}	7.26×10^{6}	3.55
Eridanus II	$5.4^{+5.6}_{-2.6} \times 10^{8}$ a	$8.3^{+1.7}_{-1.4} \times 10^4 \mathrm{b}$	$0.277 \pm 0.014^{\circ}$	-2.38 ± 0.13 ^d	$6.9^{+1.2}_{-0.9}$ d	$5.5^{+2.0}_{-2.2} \times 10^{8}$ a	$7.9^{+1.6}_{-1.5} \times 10^{6}$ a	ı

Table 2. Overview of the parameter grid used for the NBODY6DF simulation suite. From left to right, the columns give: the initial star numbers in the cluster and the corresponding total mass; the initial 3D half-mass radius used to initialize the cluster; the initial galactocentric distance of the cluster orbit; the initial tangential orbital velocity; and the central slope parameter γ of the Dehnen model used for the host potential (where $\gamma = 0$ is a core and $\gamma = 1$ is a cusp), alongside a description of the potential. In total, this table describes 960 unique simulations.

N	$M_{ini} \; [M_{\odot}]$	R _{halfmass,ini} [pc]	$R_{\rm g,ini}$ [pc]	$v_{\rm ini}/v_{\rm circ}$	Host γ	Description
216	4.18×10^{4}	2.5	45	1	1	Halo1459 DMO: pristine ΛCDM cusp
2^{15}	2.08×10^{4}	5	100	0.75	0.75	Halo1445: weakened cusp
2^{14}	1.00×10^{4}	10	200	0.50	0	Halo1459: partial core
2^{13}	5.14×10^{3}	15	_	0.25	0	Halo1459 GM:Later: partial, time-evolving core
					0	Fcore: full core

to predict the probability distribution function of their initial sizes, masses, and orbits. For these reasons, we model the SCs instead with follow-up simulations using an accurate direction summation code, NBODY6DF. We describe these follow-up simulations, next.

2.2 Direct summation N-body simulations

We simulate the evolution of SCs in the EDGE dwarfs using a variant of the NBODY6 code (Aarseth 1999) – a graphics processing unit (GPU) enabled direct *N*-body simulation tool (Nitadori & Aarseth 2012), which uses regularization to model multiple-order stellar encounters. Stellar evolution is implemented with the standard 'Eggleton, Tout and Hurley' option in NBODY6 (Eggleton, Fitchett & Tout 1989; Tout et al. 1997; Hurley, Pols & Tout 2000; Hurley, Tout & Pols 2002; Hurley 2008).

Our chosen variant is NBODY6DF⁵ (Petts, Gualandris & Read 2015; Petts, Read & Gualandris 2016), which introduces the effects of dynamical friction (first described in Chandrasekhar 1943). Dynamical friction is a drag force which acts on a body as it passes through a background of lighter bodies, and would normally manifest as a result of interactions between a SC and background stars, gas, and dark matter. NBODY6DF uses a semi-analytic approach to calculate the orbital decay of a SC due to dynamical friction against the background, eliminating the need to simulate the full galactic context. The code relies upon a distribution function to calculate the dynamical friction force, which is analytic for a Dehnen potential (Dehnen 1993):

$$\rho_{\rm Dehnen}(r) = \rho_0 \left(\frac{r}{r_{\rm s}}\right)^{-\gamma} \left(1 + \frac{r}{r_{\rm s}}\right)^{\gamma - 4},\tag{1}$$

where ρ_0 is the central density, r_s is the scale radius, and γ is a variable used to set the logarithmic slope of the inner density profile ($\gamma=0$ corresponds to a core and $\gamma=1$ corresponds to a cusp). A range of options for the variable γ are already implemented in NBODY6DF based on the analytic solutions from Dehnen (1993). As such, we make use of these by fitting the Dehnen profiles to the EDGE dwarf density profiles, as described in Section 3.1.3.

Critically, the semi-analytic dynamical friction model in NBODY6DF is able to reproduce the 'core-stalling' phenomenon whereby dynamical friction ceases when the orbital radius of the SC approaches its tidal radius (Goerdt et al. 2006, Read et al. 2006b, 2010; Petts et al. 2015, 2016; Kaur & Sridhar 2018; Banik & van den Bosch 2021). For a Dehnen potential, this radius can be estimated as:

$$r_{\text{stall}} = \left[\frac{M_{\text{SC}}}{M_{\text{g}}} \left(r_{\text{s}}^{2-\gamma} + r_{\text{s}} \gamma \right) \right]^{1/(3-\gamma)}, \tag{2}$$

where $M_{\rm SC}/M_{\rm g}$ is the ratio of the SC mass to the host galaxy mass.

The initial conditions for each SC were constructed with the tool MCLUSTER (Küpper et al. 2011) using a spherical Plummer density model (Plummer 1911) and a Kroupa IMF (Kroupa 2002; Küpper et al. 2010) with stellar masses in the range $0.1 \leq M_{\odot} \leq 100$. This corresponds to a mean stellar mass of $\approx 0.63\,M_{\odot}$. We use an initial mean metallicity of 1×10^{-4} , the lowest available in native NBODY6. We assume zero primordial binaries and that stars which evolve into black holes have no natal kick velocity. Both of these choices remove potential sources of dynamical heating and so maximize SC survivability. We retain unbound stars in the full integration of the system as we find that mass-loss rates are slightly reduced. All our SCs survive longer than a Hubble time when simulated in isolation.

We create initial conditions for SCs over a grid of masses (star numbers: $N = 2^{13}$, 2^{14} , 2^{15} , 2^{16} , yielding the initial masses given in Table 2), initial half-mass radii ($R_{1/2}$ /pc = 2.5, 5, 10, 15), orbital radii ($R_{\rm g}$ /pc = 45, 100, 200), and orbital eccentricities ($v_{\rm ini}/v_{\rm circ} = 0.25$, 0.50, 0.75, 1.00), where $v_{\rm circ}$ is the circular velocity in a Dehnen potential:

$$v_{\rm circ}^2(r) = \frac{GM_{\rm g}r^{2-\gamma}}{(r+r_{\rm s})^{3-\gamma}}.$$
(3)

The combinations of initial parameters are described in Table 2. Each permutation was then inserted into a background potential described by spherically symmetric Dehnen profile fits, which are discussed further in Section 3.1.3. These profile fits were chosen to represent a variety of central density slopes. Each simulation in the suite was run for either a Hubble time (13.8 Gyr) or until SC dissolution, which was determined as the time when the number of bound cluster stars drops below 10.

The centre of each SC was determined using the mass-weighted shrinking spheres method of Power et al. (2003), limited to stars with masses ${\leqslant}\,10\,\rm M_{\odot}$. All luminosities were converted to V-band with bolometric corrections based on fits from Reed (1998), after which we performed a cut on stars with luminosities $0.1 \geq L_V/L_{\odot,\,V} \geq 100$. This is because overly bright stars are normally removed from observational analysis, and faint stars escape detection. Halflight radii were calculated with bootstrapping analysis based on the total bound V-band luminosity. Black holes and compact remnants were excluded from our analysis when calculating optically derived values, such as the half-light radius.

Note that, although it is most similar to EriII's observed properties (see Table 1), we do not consider SC survival within Halo1459 GM:Latest. This is because, due to a late low-stellar mass, cuspy merger, its final density profile ends up being rather cuspy (see the discussion of this in Orkney et al. 2021). As such, its behaviour in terms of SC survival is already covered by Halo1445. None the less, it would be interesting to explore this galaxy further in future work. It has a half-light radius and stellar content similar to EriII,

⁵https://github.com/JamesAPetts/NBODY6df

precisely because it assembles late from many minor mergers (see Rey et al. (2019)). These minor mergers themselves may interact with the central SC, potentially explaining some of its puzzling properties. Exploring this is beyond the scope of this present work.

3 RESULTS

3.1 Cosmological simulations

3.1.1 EDGE ultra-faint dwarf candidates

The key observational properties of our EDGE UFDs are presented in Table 1. For comparison, we include properties for the UFD EriII, with values taken from the literature. The chosen EDGE galaxies are selected because they compare best to EriII in terms of their virial mass, stellar mass, and their status as isolated reionization fossils, but they are not intentionally designed to resemble EriII. Indeed, the EDGE stellar masses are somewhat greater than the upper limit measured for EriII. Notice that for Halo1459, the stellar mass and stellar metallicity drop as formation time is delayed (see GM:Later and GM:Latest). A delayed formation time also leads to a larger half-light radius and stellar velocity dispersion. These trends are a direct result of the assembly history and are described fully in Rey et al. (2019). The later forming versions of Halo1459 approach more and more closely the observed properties of EriII in just about every respect – M_* , $R_{1/2}$, [Fe/H], σ_{LOS} and even the dynamical mass within $R_{1/2}$. This suggests that EriII is likely a late-former, following the arguments in Rey et al. (2019), which could be key to understanding its puzzling SC.

In our EDGE simulations, galaxies that form later are larger and have lower metallicity because their stellar content comprises a larger fraction of accreted stars. This is why, as we genetically engineer Halo1459 to form later, its size grows and its metallicity drops (Rey et al. 2019). Note, however, that forming late is not sufficient on its own. Halo1445 forms even later than Halo1459 GM:Latest, yet its half stellar mass radius is a relatively compact 100 pc. This occurs because Halo1445 forms late but from fragments that have little/no stellar mass. Hence, its resulting size remains compact, while its metallicity is not as low as Halo1459 GM:Latest. For the above reasons, the galaxies drawn from EDGE that are most similar to EriII are those that form late and whose stellar populations comprise a high fraction of accreted stars, like Halo1459 GM:Latest. We expect these trends would be replicated across different simulations, although alternative galaxy-formation models may find that EriII is better-matched by galaxies with a median assembly history, with late assemblers being even larger and more metal poor.

3.1.2 Mass assembly and star formation

Our EDGE haloes attain M_{200c} halo masses of approximately $1.5 \times 10^9 \, \rm M_{\odot}$ by z=0, where we define M_{200c} as the mass within a spherical volume encompassing 200 times the critical density of the universe. All haloes form stars when baryonic physics is switched on, although this star formation is confined to early times (z>4). Star formation continues for some time after the onset of reionization, but is quenched after the remaining cool gas within the halo is exhausted (as shown in Rey et al. 2020, and see also Susa & Umemura 2004; Oñorbe et al. 2015).

The star formation (left-hand axis) and mass growth histories (right-hand axis) are shown in Fig. 1 up to z=3. The mass growth is defined as the mass enclosed within 1 kpc rather than the virial mass M_{200c} , because the central mass is what is most important

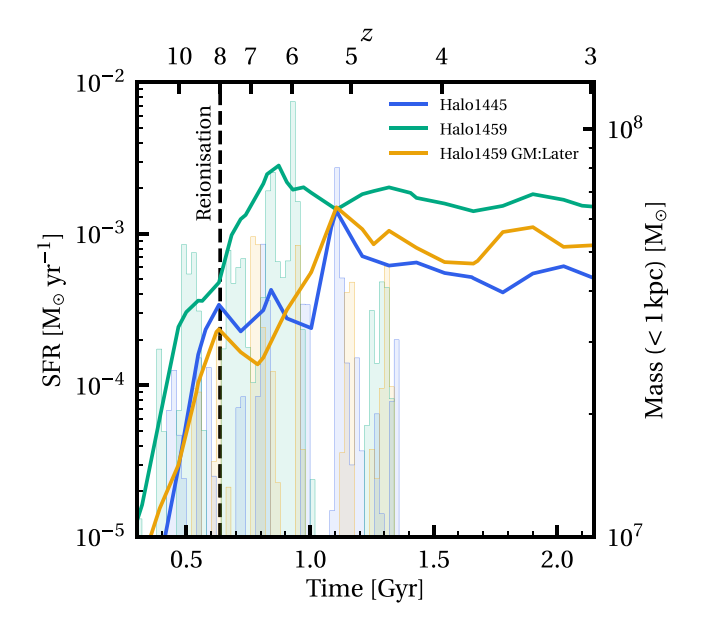


Figure 1. The star formation rate (left-hand y-axis, histogram) and mass assembly history (right-hand y-axis, lines) for our EDGE UFD simulations, at early times. The star formation rate is averaged over bin sizes of 0.02 Gyr and takes into account all stars formed within the virial radius R_{200c} of the main progenitor halo. The mass assembly history considers the total mass contained within the inner 1 kpc of the main progenitor halo. A dashed line indicates the start of reionization. The dwarfs continue to form stars until their remaining cold gas is depleted (see Rey et al. 2020). Only more massive EDGE dwarfs (not included in this paper) are able to accrete sufficient gas after reionization to reignite star formation.

for the survival of low-orbit SCs, and because M_{200c} undergoes a pseudo-growth due to the lowering background density of the Universe as it expands (Diemand, Kuhlen & Madau 2007; Diemer, More & Kraytsov 2013). The mass enclosed within 1 kpc remains roughly constant after 1 Gyr, despite the continued accretion of dark matter. The star formation in all haloes is bursty, which is a necessary quality in driving the gaseous flows responsible for dark matter core formation (Pontzen & Governato 2012). Indeed, we observe a fluctuating central gas mass in all haloes at early times (Orkney et al. 2021). Halo1459 assembles its central mass most rapidly and has the highest final central mass, along with the most substantial star formation. The larger dynamical potential well aids in the compression of gas into star-forming clouds. This is a consequence of the well-established concentration-formation relation (e.g. Wechsler et al. 2002; Ludlow et al. 2014; Wang et al. 2020a).

3.1.3 Density profiles

In Fig. 2, we present spherically symmetric Dehnen profile fits to the total mass distribution of our EDGE haloes after the cessation of star formation. The raw density profiles of the dark matter distribution were reported previously in Orkney et al. (2021). For Halo1445 and Halo1459, we fit the halo density profiles at z=3.2, by which time the inner halo is fully assembled and stable until z=0 (see Fig. 1). For Halo1459 GM:Later, which experiences additional late time heating from minor mergers, we make a fit both at z=4 and z=0, interpolating between them to obtain a time varying potential that matches the simulation data at all times (using the method described in Orkney et al. 2019). We also produce a fit for Halo1459

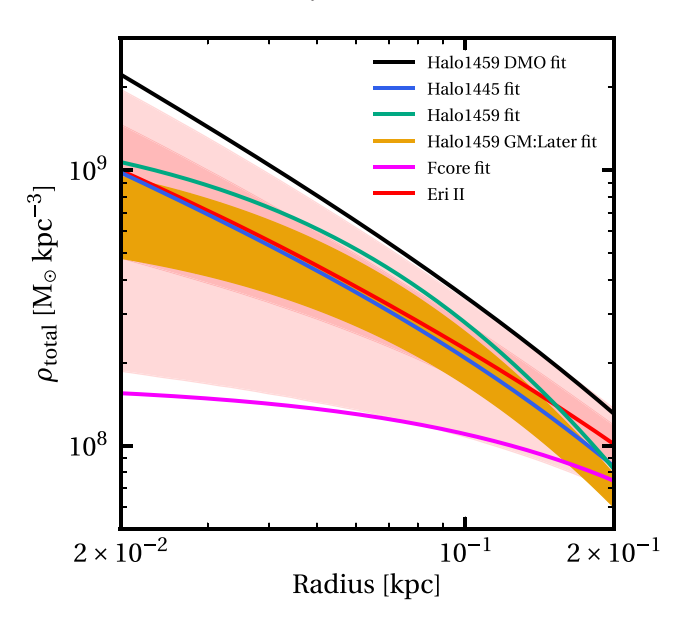


Figure 2. Fits to the total inner 3D density profiles of EDGE haloes at z = 3.2. The fits to Halo1459 GM:Later are shown as a filled region, with the upper (lower) limit representing the fit at z = 4 (z = 0). We also show constraints on the density profile of EriII based on the 'core + tides' profile fit from Zoutendijk et al. (2021a), where the dark and light shaded bands correspond to the 68 per cent and 95 per cent confidence limits, respectively.

DMO at z=3.2 to provide a $\gamma=1$ cusp reference, but do not fit profiles to the other DM-only simulations. These fits are produced with the PYTHON module LMFIT (Newville et al. 2016), considering only the portion of the profile that is unaffected by numerical relaxation (as discussed in Orkney et al. 2021, Appendix A). Our fits accurately reproduce the simulation density over the ranges shown, but deviate from the data in the outer regions because a Dehnen profile density falls off as r^{-4} in its outskirts whereas our simulated haloes fall off as r^{-3} . These fits are, none the less, suitable for our purpose here, since we limit our analysis to initial orbital radii of 200 pc or less.

Included in Fig. 2 is the cored Dehnen profile from Contenta et al. (2018). Those authors found that SCs evolving in this profile were best able to match the properties of the SC in EriII. Hereafter we refer to this profile as 'Fcore'; it has a substantially lower density core than any of our EDGE haloes. We also show observational constraints on the dark matter density profile of EriII in red, based upon the 'core + tides' fit performed by Zoutendijk et al. (2021a), assuming a CDM cosmology. This fit is made with pyGravSphere (Read & Steger 2017) using stellar line-of-sight velocities as measured by the MUSE-Faint survey. The shaded bands correspond to 68 per cent and 95 per cent confidence limits. The Dehnen profiles fit to our EDGE dwarfs are mostly contained within the 68 per cent limits, and the Fcore profile sits at the edge of the 95 per cent limits. Therefore, the profiles we consider are well bracketed by observational fits.

3.2 *N*-body star cluster simulations

3.2.1 SC properties after a Hubble time

We find that only those SCs hosted by cored potentials (models: Halo1459, Halo1459 GM:Later and Fcore) survive for a full Hubble time. Just two SCs in a weakened cusp potential (Halo1445) survive longer than 6 Gyr, while only three SCs in the pristine cusp potential

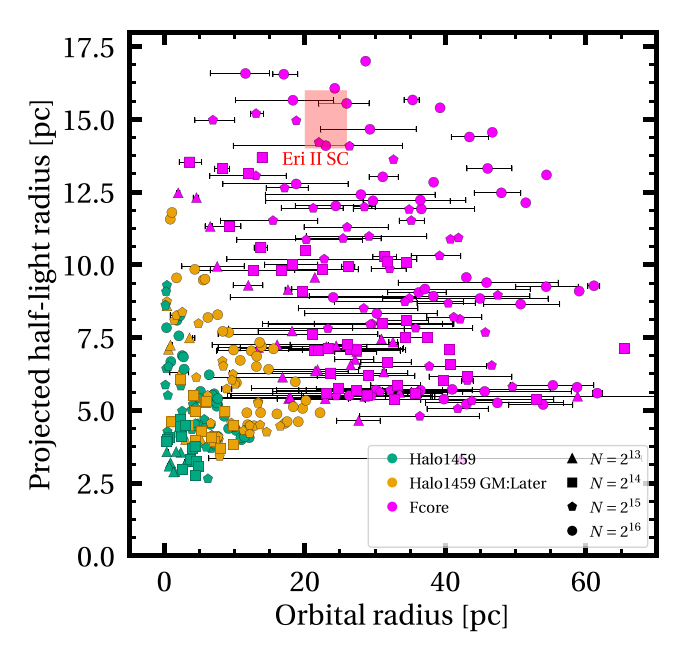


Figure 3. The projected half-light radius versus the orbital radius of all surviving SCs from our simulation suite after a Hubble time. The marker style indicates the initial number of stars, *N*, in each SC, while the colour indicates the host mass profile model, as marked in the legend. Each point represents the average projected half-light radius of the current SC orbit, with the 'error bars' marking the orbital apocentre and pericentre. Also included is a red box marking the properties of the SC in EriII Simon et al. (2021). No SCs from Halo1445 or Halo1459 DMO survive after a Hubble time and so these two host potentials do not appear on the Figure. A small number of SCs in the Fcore potential lie beyond the 70 pc limit of this plot.

(Halo1459 DMO) survive longer than 3 Gyr. Therefore, we confirm the results of prior work that SC survival is extremely sensitive to the inner potential slope of the host (e.g. Amorisco 2017; Contenta et al. 2018; Orkney et al. 2019).

The projected half-light and orbital radius of all surviving SCs are presented in Fig. 3. The values are averaged over the last pericentre-apocentre passage, where the most recent pericentre and apocentre are marked by the horizontal 'error bars'. The observed properties of the SC in EriII, with uncertainties, are indicated by a red box.

The orbital response to dynamical friction is so strong that the majority of SCs approach to their core-stalling limit within a few Gyrs. However, some SCs in the Fcore potential have yet to reach this limit by a Hubble time. The orbital radius then continues to decay as the SC is stripped of mass, as predicted by equation (2). SCs inhabiting the Fcore potential adopt a wider range of final orbital radii depending on their initial orbits and retain a larger degree of their initial orbital eccentricity, whereas the orbits of SCs in other host potentials are rapidly circularized. Despite a stronger dynamical friction force, the most massive SCs maintain slightly higher final orbital radii due to their larger core-stalling radius.

As found in prior work, SCs within the Fcore model grow to significantly larger sizes due to the low background potential and reduced tidal stripping (Contenta et al. 2018). Amongst these, the very largest SCs are those with the largest $R_{\rm halfmass,ini}$, with $R_{\rm halfmass,ini} = 15$ pc bracketing the size of the SC in EriII.

Following the premise that harsher gravitational tides act to destroy orbiting SCs more rapidly, it is natural to assume that there are simple relationships between SC survival and the initial orbit. Normally, it is expected that more eccentric orbits, which plunge the SC in and out

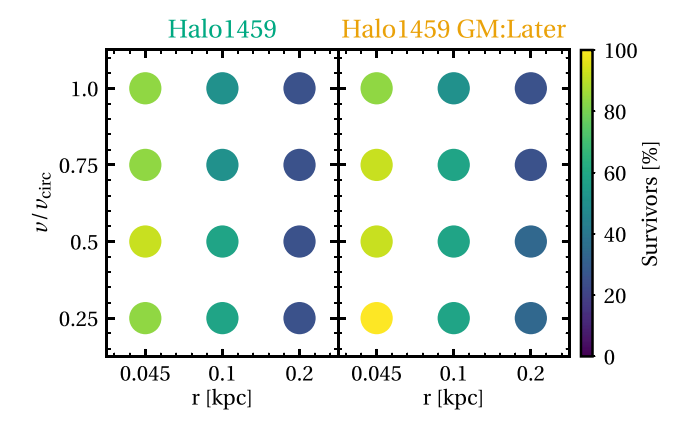


Figure 4. The Hubble time survival of SCs in two host potentials. Each circle represents the survival percentage of SCs in Halo1459 and Halo1459 GM:Later, partitioned by initial velocity and orbital radius. We have omitted SCs with $R_{\text{halfmass,ini}} = 15 \,\text{pc}$ because these rarely survive, regardless of their initial orbital parameters.

of a stronger background potential, result in shorter-lived SCs due to the impact of tidal shocks (Weinberg 1994; Kundic & Ostriker 1995; Gnedin, Hernquist & Ostriker 1999; Baumgardt & Makino 2003; Webb, Reina-Campos & Kruijssen 2019). To explore this, in Fig. 4 we compare the survival of a selection of SCs in the Halo1459 and Halo1459 GM:Later host potentials, grouped by initial orbital velocity and radius. As expected, survival is improved with lower initial orbital radii. However, survival is largely independent of initial orbital eccentricity, with variation mostly below the level of Poisson noise.

Whilst it is generally the case that eccentric orbits encourage SC dissolution, it is also the case that dynamical friction is enhanced on eccentric orbits (which in turn acts to circularize the orbit). If the orbit of a SC decays to within the core region of the host potential, which typically occurs over Gyr time-scales, then it is better able to survive. In the case of the host potentials considered here, these two competing processes balance each other remarkably well. This is not the case for our steeper host potentials (models: Halo1445 and Halo1459 DMO), in which SCs survive the longest when on more circular orbits.

3.2.2 SC shape after a Hubble time

The ellipticity of the SC in EriII is $0.31^{+0.05}_{-0.06}$ (Simon et al. 2021), which is exceedingly high when compared to Milky Way globular clusters (Harris 2010). In this section we investigate the shapes of our simulated SCs in terms of their ellipticity and orientation. We define the ellipticity, e, as 1 - b/a, where a and b are the longaxis and short-axis of an ellipse fit to the SC stars. The orientation, θ , is defined as the inclination in the long-axis of the SC ellipse with respect to the centre of the host potential (and is distinct from the 'alignment' measurement reported in Simon et al. 2021). Both values are calculated in projection, and are consistent with literature definitions. Our calculations are performed with the shape finder in PYNBODY, modified for use with projected stellar distributions. We perform bootstrapping analysis over 1000 iterations for every shape fit, generally finding low uncertainties except for the degenerate orientation angles of near-circular SCs. We investigate the robustness of our method in Appendix A, and show that it compares well to a typical observational method.

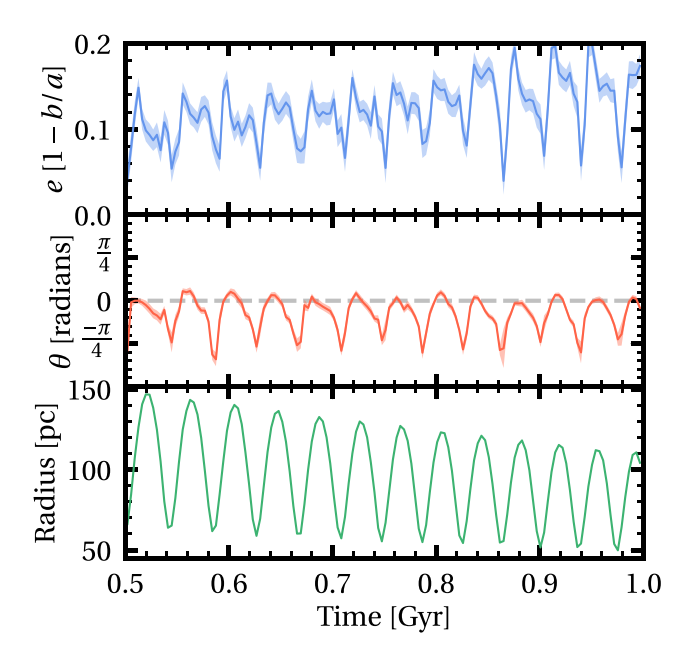


Figure 5. The evolution of the SC shape for a single example simulation over 0.5 Gyr (from 0.5–1 Gyr in simulation time). The upper panel shows the ellipticity e, the middle panel shows the orientation θ (where $\theta=0$ is aligned with the galactic centre), and the lower panel shows the galactocentric orbital radius. The filled regions are the 1σ uncertainty determined from bootstrapping. For eccentric orbits, the SC shape and orientation is highly dependent on the position along the orbit.

Throughout, we orient our SCs face-on to the orbital plane. This does not materially affect our results and conclusions. We explore this explicitly in Appendix B, where we consider the other extreme of orienting the SCs edge-on to the orbital plane. In this case, we find that tidally stripped debris along the line of sight can generate higher ellipticities (with a secondary sub-dominant effect caused by tidal compression). However, this occurs only for models in which the SCs are too small and not offset enough to be consistent with the SC in EriII.

In Fig. 5, we show the evolution of the ellipticity e and the orientation θ for one example SC over a Gyr. The initial properties of our chosen example are $M_{\rm ini}=2.08\times10^4\,{\rm M_\odot}$, $R_{\rm halfmass,ini}=5\,{\rm pc}$, $R_{\rm g,ini}=200\,{\rm pc}$, and $v_{\rm ini}/v_{\rm circ}=0.50$, orbiting in the Halo1459 model. The SC undergoes total dissolution after 1.8 Gyr. This example was chosen purely because it clearly exhibits periodic trends, but there are comparable patterns for other simulations on non-circular orbits. The figure shows that e (upper panel) and θ (middle panel) vary periodically with the orbital radius (lower panel). e is maximized at apocentre, at which time the cluster is most aligned with the galactic centre ($\theta=0$). The periodicity in e is a consequence of the tidal material sloshing around the SC body, and is strongest for simulations where there is significant tidal material. There are also sub-dominant long-term evolutionary trends in all simulations.

We show e and θ for all surviving SC simulations in Fig. 6. Motivated by the results in Fig. 5, we estimate the SC shape at the most recent orbital apocentre. The coloured Gaussian kernel density estimations show the contributions from the different host potential profiles. This shows that, whilst all SCs show a preference for aligning with the centres of their host galactic potentials, their ellipticity remains much lower than that of the SC in EriII. As anticipated in Section 1, this is because all of the surviving SCs orbit close to the centre of $\gamma = 0$ background potentials and, therefore,

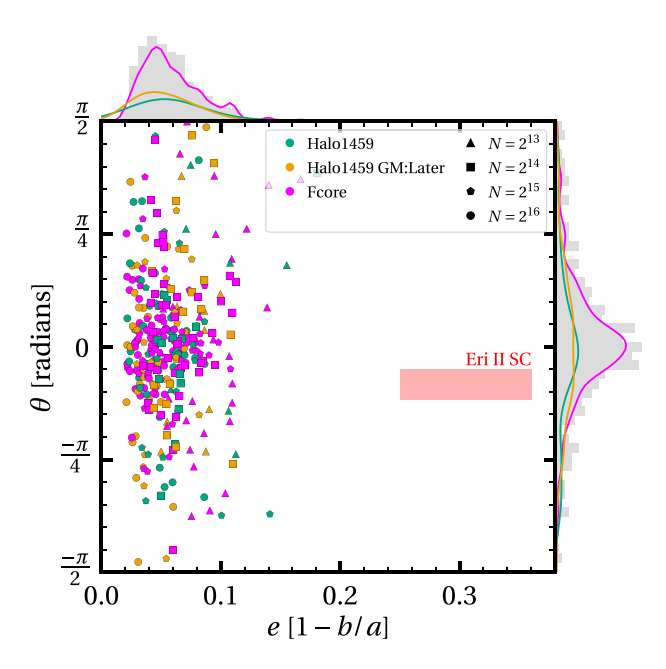


Figure 6. The orientation θ versus ellipticity e for all surviving SC simulations after a Hubble time, as viewed face-on to the orbital plane, calculated at the orbital apocentre (maximizing e and minimizing $|\theta|$). Histograms, which include Gaussian kernel density estimations for each host profile, are shown at the borders. The red region indicates the observed properties of the SC in EriII from Simon et al. (2021).

experience little tidal perturbation. We explore the implications of this in Section 4.

3.2.3 Primordial ellipticity

In Section 3.2.1 and Section 3.2.2, we have shown that SCs survive for long times in all cored potentials, while only in the shallower Fcore potential do they reach a size and offset comparable to EriII's SC. However, due to the lack of tidal forces within the core, these SCs retain their initial sphericity and fail to match the high ellipticity of EriII's SC. This appears to present a significant problem for the full core scenario since prior work suggests that any initial ellipticity in EriII's SC should be rapidly erased, given its short relaxation time (see Section 1 and Agekian 1958; Shapiro & Marchant 1976; Longaretti & Lagoute 1996; Einsel & Spurzem 1999a; Bianchini et al. 2013).

In this section, we examine the above concern in more detail. Firstly, we note that young SCs are typically born elliptical due to rotational flattening, pressure anisotropies and/or SC-SC mergers (e.g. Fall & Frenk 1983; Bianchini et al. 2018; Ferraro et al. 2018; Kamann et al. 2018), with 'primordial' birth ellipticities often higher than e > 0.3 (Getman et al. 2018). Pressure anisotropies, which arise when systems form the violent relaxation of an aspherical collapse, are lost on relaxation timescales (Aarseth & Binney 1978). Ellipticity, due to rotational flattening, should also be reduced on a relaxation time-scale as two-body scattering moves high angular momentum stars (which are responsible for the elliptical shape) to the outskirts of the cluster, where they are lost to tides (Einsel & Spurzem 1999b; Tiongco, Vesperini & Varri 2017). However, the tidal forces vanish inside a constant density core and there is no mechanism to carry away the high angular momentum material. This suggests that in a weak tidal field, primordial ellipticity should be 'locked in', surviving for long times (Goodwin 1997).

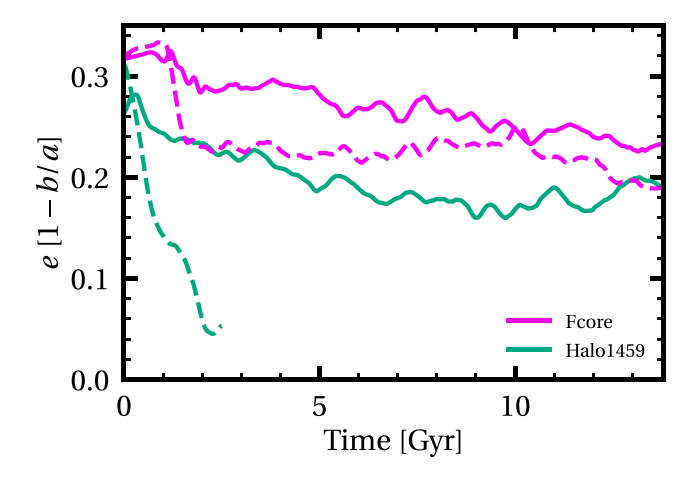


Figure 7. Evolution of the projected ellipticity for initially rotating and elliptical SCs in a partial core (Halo1459; green) and full core (Fcore; magenta) background potential. The data have been smoothed to remove periodic trends. The solid (dashed) lines represent orbits starting at a radius of 45 pc (200 pc). The SC in the 'Halo1459' potential at an initial orbital radius of 200 pc dies shortly after 2 Gyr.

To test the above idea, we deform one of our SCs and add a rotation curve about the deformation axis of the following form:

$$v_{\rm rot} = \frac{2V_{\rm peak}}{R_{\rm peak}} \frac{R}{1 + (R/R_{\rm peak})^2},\tag{4}$$

where V_{peak} is the maximum velocity and R_{peak} is the radius of maximum velocity (as in Lynden-Bell 1967; Mackey et al. 2013). We ensure that virial equilibrium and the overall SC volume are maintained. Through this, we create a SC with $M_{\rm ini} = 2.08 \times 10^4 \, {\rm M_{\odot}}$, $R_{\text{halfmass,ini}} = 5$, $e_{\text{ini}} = 0.31$ and rotation with a peak of 1.75 km s⁻¹ at the half-mass radius. In Fig. 7, we show the evolution of the ellipticity of this SC when evolved in two different background potentials. In both cases, we initialize the SC on a circular orbit at two different initial orbital radii of 45 pc (solid lines) and 200 pc (dashed lines). A high ellipticity is maintained for over a Hubble time in the Fcore potential, and is rapidly lost in the Halo1459 potential when at an initial offset of 200 pc. This suggests that the high ellipticity of EriII's SC does not in fact present a problem for the Fcore model. In such a model, it must simply reflect the ellipticity of EriII's SC at birth, which would be consistent with that of young SCs (Getman et al. 2018). Given the much larger parameter space required to explore the ellipticity and orbit of EriII's SC, we leave a more thorough investigation of how ellipticity affects the survival and evolution of SCs to future work.

3.2.4 Star clusters in ultra-faint dwarfs via recent accretion

We now explore an alternative scenario for EriII's SC in which it has been recently accreted rather than surviving with its current properties for long times. Whilst our EDGE dwarfs assemble their central mass by z=4, there are still a significant number of mergers throughout their lives. Indeed, EriII is most similar to the very latest assembling EDGE dwarfs (see Section 3.1.1 and Table 1). These mergers can contribute to late time dark matter heating as with Halo1459 GM:Later (Orkney et al. 2021), but could also act as vehicles for depositing SCs. There are a total of five star-rich mergers which occur after z=1, however only one is massive enough to compare favourably to the SC in EriII. A SC that is donated via a sub-halo merger would be protected from much of the destructive

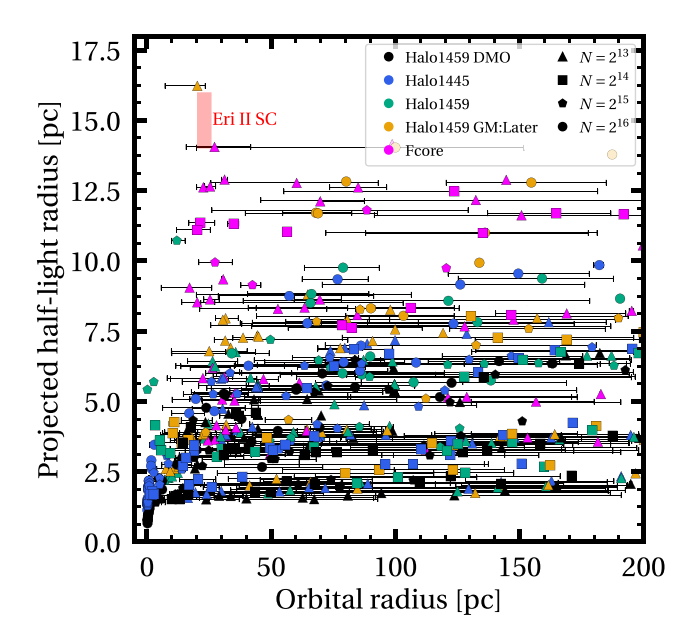


Figure 8. The projected half-light radius versus the orbital radius of our SCs simulation suite, shown at the time in their evolution when they pass the lower mass estimate for the SC in EriII. The figure format is otherwise identical to that of Fig. 3.

forces of gravitational tides until the dark matter envelope is stripped (e.g. Mashchenko & Sills 2005a, b; Boldrini & Vitral 2021; Vitral & Boldrini 2021). The increased system mass would also cause the SC orbits to decay faster due to dynamical friction. Assuming that previously accreted SCs fall to the centre of EriII without yielding a detectable central SC (cf. Shao et al. 2021), it is possible that EriII experienced a long chain of such accretions of which only the most recent remains detectable.

So far, we have considered only SCs which have survived within their host potential for a Hubble time, but recently accreted SCs would not need to survive this long. Here, we instead consider SCs at a time when their bound mass drops just below the lower mass estimate of the SC in EriII (which we take to be $2.5 \times 10^3 \,\mathrm{M}_{\odot}$, following Crnojević et al. 2016; Contenta et al. 2018), with the one additional constraint that they survive for at least 100 Myr. Many of the SCs in this low-mass regime have been exposed to their host potentials for only a short time, and are close to total dissolution. In Fig. 8, we once again show the projected half-light radius against orbital radius. Since we are now, including SCs that are close to dissolution from tides, there are contributions from SCs in the steeper background potential models (models: Halo1459 DMO and Halo1445). Notice, however, that the half-light radii of the SCs in these steeper potentials never grow beyond $\sim 10 \,\mathrm{pc}$ and so they remain inconsistent with EriII's SC. In Fig. 9, we once again show e and θ . There is now a spray of SCs at higher e, predominantly formed by simulations in the densest potentials. There are also a small number of highly elliptical SCs in the Fcore potential, which are diffuse SCs with high $R_{halfmass,ini}$ and are therefore more sensitive to gravitational tides. The spray is clustered around an orientation of $\theta = 0$ at low e, but then begins to favour more misaligned θ at increasingly high e. This is because the presence of tidal tails contribute to the measured ellipticity, and these originate at the Lagrange points of the SC (which are always aligned with the galactic centre; e.g. Klimentowski et al. 2009). As the tidal tails grow longer they begin to trail and lead the SC orbit, which leads to a higher

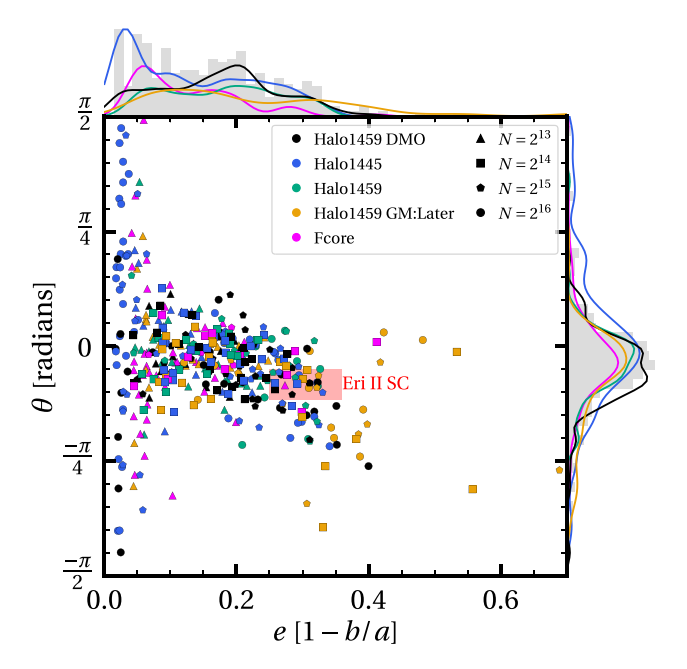


Figure 9. The orientation θ versus ellipticity e for our SCs simulation suite, shown at the time in their evolution when they pass the lower mass estimate for the SC in EriII. The figure format is otherwise identical to that of Fig. 6.

perceived *e* and a larger orientation angle with respect to the galactic centre. We discuss the implications of this phenomenon, next.

3.2.5 Star cluster tidal tails

The SC ellipticities and orientations presented in Figs 6 and 9 are as viewed in the plane of the SC orbit. However, the SC orbit in EriII may be viewed from an edge-on perspective, or somewhere inbetween. This could change the perceived orientation and ellipticity.

We illustrate this key point in Fig. 10, which shows an example SC simulation at orbital apocentre (thereby maximizing its ellipticity). The left-hand panels show the SC at an early stage in its evolution. At this time, it is well aligned with the centre of the host potential and has only a low tidal tail brightness. The ellipticity ($e \approx 0.2$) is clear when viewed face-on to the orbital plane (upper panel), but is diminished ($e \approx 0.07$) when viewed edge-on to the orbital plane (lower panel). The right-hand panels show the same SC in the final few Myrs before dissolution, at which stage it grows long tidal tails. These long tidal tails begin at the Lagrange points of the SC, then trail and lead the orbit. This leads to a shape fit that is highly elliptical ($e \approx 0.48$) and misaligned with the centre of the host potential when viewed face-on to the orbital plane (upper panel). The SC now continues to appear highly elliptical ($e \approx 0.53$) when viewed edge-on to the orbital plane (lower panel).

The presence of tidal tails, long or short, means that the apparent ellipticity will increase when considering larger cluster-centric radii, a behaviour that has been reported for EriII's SC (see the discussion in section 4 of Simon et al. 2021). However, even our lowest mass SC simulations in this 'recent accretion' scenario possess tails with surface brightness comparable to or exceeding the central brightness in EriII (27.2 mag/arcsec²; Crnojević et al. 2016) and should therefore be present in the observations of the galaxy. Yet, there is no sign of tidal material beyond two-times the half-light radius of the SC (see Fig. 11, Simon et al. 2021). This appears to rule out recently accreted SCs where the high ellipticity is due to significant tidal disruption.

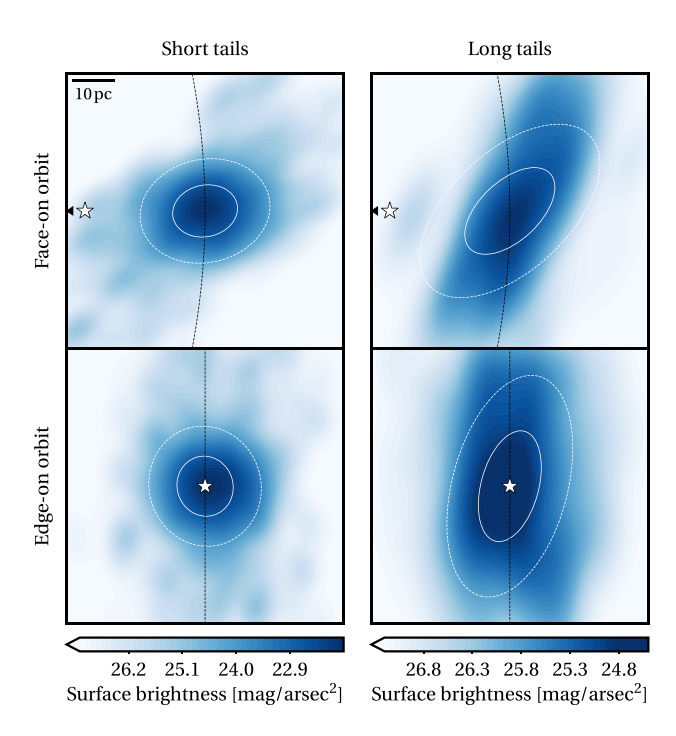


Figure 10. Kernel density estimate plots of the *V*-band surface brightness for a SC simulation at two stages in its evolution, shown with two different orientations. A surface brightness background of $27.2 \, \text{mag/arcsec}^2$ is included to mimic the central brightness of EriII (Crnojević et al. 2016). The white star indicates the centre of the host potential, a black dashed line represents the SC orbit, and white solid/dashed lines represent a shape fit to the SC shown at $1 \times /2 \times$ the half-light radius. The left-hand panels represent a younger SC with relatively short tidal tails coming from the Lagrange points. The right-hand panels represent the SC on the verge of total dissolution, which has become smeared across its orbit.

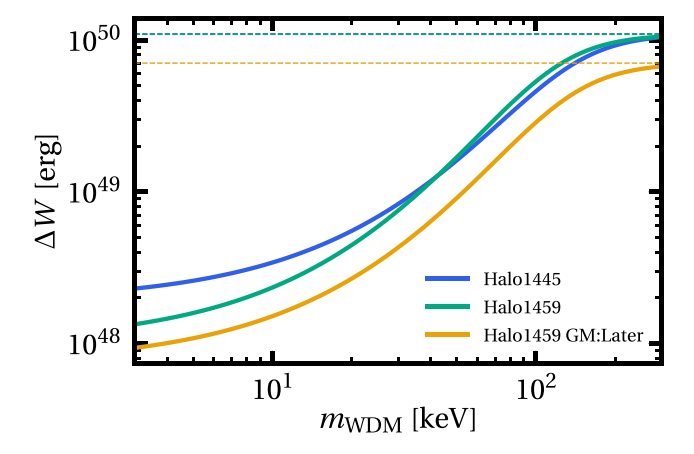


Figure 11. The energy (ΔW) required to transform a central cusp into coreNFW profiles fit to EDGE galaxies at z=4 (see Appendix C for details of how this is calculated). The halo concentration parameters have been varied, corresponding to WDM over a range of particle masses. Horizontal dashed lines mark the values of ΔW from Table C1, which shows the energy required to lower the central density cusp in a CDM cosmology.

4 DISCUSSION

4.1 A full dark matter core in EriII

We have shown that a substantial dark matter core allows for the stable existence of large, elliptical, and radially offset SCs, like that seen in EriII, over many Gyrs. Such a core would support both *in situ* and accreted SCs. However, none of the UFDs in EDGE produce a central dark matter core of sufficient size and low enough density. We discuss next how such a large, low density, core might arise.

4.1.1 Growing a full dark matter core

4.1.2 Full cores in ∧CDM

In Orkney et al. (2021), we showed that haloes with significant early star formation and late minor mergers are the most likely to have shallow inner dark matter density profiles in EDGE. However, none of the EDGE dwarfs considered here lie outside of the 68 per cent confidence intervals of mass assembly histories in Λ CDM: they are all rather common. Rarer haloes could conceivably grow larger dark matter cores (though this is not guaranteed). We will consider this possibility in future work.

Alongside rarer assembly histories, we should also consider the sensitivity of dark matter core formation to the sub-grid baryonic physics model. Pontzen et al. (2021) find that a very small increase in the burstiness of star formation (and therefore, in the mass of inflowing and outflowing gas) can form a substantial dark matter core in an UFD – rather similar to the Fcore model we have explored here – without significantly increasing its stellar mass. Thus, it is possible that going to even higher numerical resolution, or including further physics not currently modelled in EDGE, could lead to the formation of larger dark matter cores in UFDs in ACDM.

4.1.3 Full cores in AWDM

A full dark matter core could also indicate a departure from a ΛCDM cosmology. One possibility is warm dark matter (WDM). While WDM does not in itself produce significant dark matter cores, it does lower the concentration of dark matter haloes such that core formation via baryonic effects is more easily facilitated (Macciò et al. 2012; Fitts et al. 2019). In Fig. 11, we quantify the energy required to form cores in AWDM as compared to ACDM, all other things being equal. Specifically, we show the energy difference $(\Delta W$, as calculated in Appendix C) between cuspy and dynamically heated potential profile fits, but varying the concentration parameter c according to predictions for a thermal relic WDM particle (as in Schneider et al. 2012). Notice that ΔW plummets by ~ 2 orders of magnitude for the lowest WDM particle masses (we truncate the figure at $m_{\rm WDM} = 3 \, \rm keV$ since this is the conservative limit set by recent data constraints; e.g. Banik et al. 2021; Enzi et al. 2021; Nadler et al. 2021). However, there is an important caveat here that the reduction in central density in WDM as compared to CDM could also result in delayed star formation (as in Lovell et al. 2020) - which would make core formation more difficult again. Secondly, the halo formation time, and therefore the final stellar mass, are different in a WDM cosmology (i.e. Elahi et al. 2014; Dhoke & Paranjape 2021). We will consider these points using dedicated WDM simulations, in future work.

4.1.4 Full cores in ΔSIDM

The presence of a dark matter core in EriII could point to a self-interacting dark matter (SIDM) cosmology. In some models, thermalization occurs due to scattering between dark matter particles within dense halo centres. This leads to a density core that grows with time. Read et al. (2018) find that 'coreNFW' density profiles (Read

et al. 2016) provide an excellent match to the form of haloes in simulations of a velocity-independent SIDM cosmology, assuming interaction cross-sections within the range of current observational constraints. Using the methodology described in §3.2 of Read et al. (2018), which is calibrated to the Vogelsberger, Zavala & Loeb (2012) SIDM cosmological simulations, we find that an interaction cross-section of $> 0.28~\text{cm}^2/\text{g}$ is sufficient to lower the central density of our dwarf galaxy simulations as far as the Fcore model. Interestingly, this is consistent with the latest constraints on SIDM from dwarf galaxy scales (e.g. Read et al. 2018; Correa 2021).

In other SIDM models, core formation proceeds via dark particle annihilation in dense halo centres. In Zoutendijk et al. (2021b), an annihiliation cross-section is derived based on observational fits to the density profile of EriII assuming the velocity-independent SIDM model of Lin & Loeb (2016). The lower-bounds of this fit are not dissimilar to the Fcore model. Following Zoutendijk et al. (2021b), the annihilation cross-section $\sigma/m = \Gamma/2v$, where v is the typical velocity. We find that an annihilation cross-section of $\sigma/m < 1.7 \times 10^{-35} (f/10)^{-1} (v/10 \, \text{km}^{-1})^{-1} \, \text{cm}^2 \, \text{eV}^{-1} c^2$ is sufficient to lower the central density of our dwarf galaxy simulations as far as the Fcore model, which is roughly a factor of four greater than the 95 per cent confidence constraint derived in Zoutendijk et al. (2021b).

4.2 A recently accreted SC in EriII

An alternative model to the 'full core' scenario explored above is that EriII has a partial core. However, a SC in this model is unlikely to survive a Hubble time without falling into the potential centre. Instead, the SC must be recently accreted, perhaps via a late minor merger. Then, an inflated half-light radius may be attained as the SC approaches tidal disruption. Such a donation may be entirely natural. Recall that galaxies drawn from our EDGE simulations were most similar to EriII's observed properties if they assembled late from starrich minor mergers (see Section 3.1.1 and Table 1). In this scenario, the properties of EriII's SC may owe more to the initial conditions of its orbit and mass than to the density profile of EriII's inner dark matter halo.

Firstly, we note that even in this model a 'pristine' dark matter cusp in EriII remains too destructive. As shown in Fig. 8, the Halo1459 DMO model is unable to host SCs as large as that seen in EriII, even if only momentarily. A partial core, however, as in Halo1459GM:Later can support reasonably large, offset, SCs. As shown in Fig. 9, the tides experienced by SCs disrupting in this potential can naturally generate ellipticities similar to that seen in EriII's SC. However, this same model fails to produce a size or offset compatible with EriII's SC (Fig. 8). Furthermore, it yields tidal tails bright enough that we should have seen them in current data. Therefore, the notable absence of such tails appears to be a strong indicator that the SC in EriII is not consistent with this scenario. It may be worth considering whether tidal tails could be obscured. This might occur if the tails are viewed along the line-of-sight, if the luminosity of stripped stars is lower due to mass segregation within the SC, or if the tail material is spread over a wider track. The first scenario is possible, but demands fine-tuning and an unlikely chance orientation of the SC orbit. As shown in Balbinot & Gieles (2018), mass segregation is greatest in denser SCs, which we find do not grow to the large size observed for the SC in EriII. The mass segregation for our more diffuse SCs has a negligible influence on tail brightness within the range of our luminosity cuts.

We find that tidally-induced ellipticity occurs preferentially for higher apocentre orbits (> 100 pc) than the projected offset observed for EriII's SC. It is, therefore, reasonable to question the likelihood

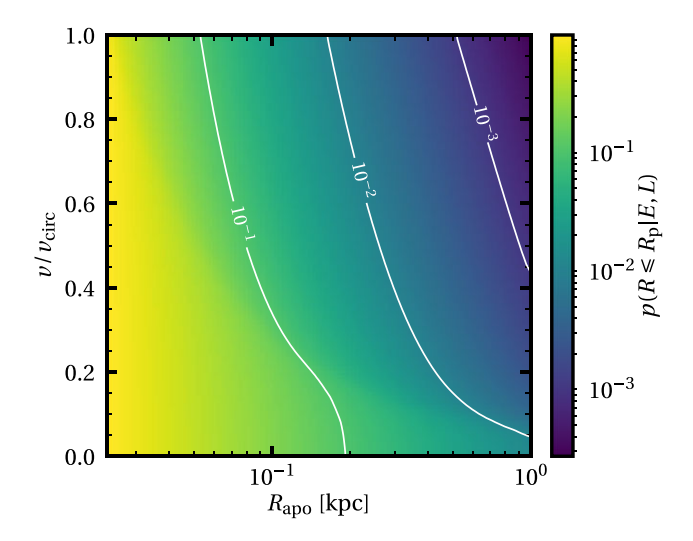


Figure 12. The probability (equation 5) of observing a SC at a projected radius $R \le R_p$, where $R_p = 23 \,\mathrm{pc}$, over a range of orbital velocities and apocentres. White lines show contours of constant probability.

of observing EriII's SC at its current projected distance if the true separation from the centre of EriII is > 100 pc. To quantify this likelihood, we calculate the probability, described in Cole et al. (2012):

$$p(R \leqslant R_{p}|E, L) = \int_{r_{peri}}^{r_{apo}} \left[1 - (1 - R_{p}^{2}/r^{2})_{+}^{1/2} \right] \times \frac{dr}{v_{r}} / \int_{r_{peri}}^{r_{apo}} \frac{dr}{v_{r}},$$
 (5)

where $r_{\rm apo}$ and $r_{\rm peri}$ are the orbital apo- and pericentre, v_r is the radial velocity and $(\cdot)_+ \equiv \max{\{0,\cdot\}}$. This gives the probability of observing an orbit at a projected radius $R \leq R_{\rm p}$, assuming a constant orbital energy E and angular momentum L. In Fig. 12, we calculate $p(R \leqslant R_{\rm 23\,pc}|E,L)$ for a grid of orbits over a range of apocentres and initial tangential velocities. The background potential is fixed to our 'Halo1459' Dehnen model, though the results are near-identical for our other background profiles. By construction, p=1 when $R \leq 23$ pc. However, p rapidly drops to $\lesssim 0.1$ beyond $R \gtrsim 100$ pc.

It may also be possible that a SC is so recently accreted to a 'partial-core' host potential that it retains both a high primordial ellipticity and large half-light radius, and is not yet greatly disturbed by gravitational tides. We find that SCs with an initial half-light radius of 15 pc are extremely vulnerable to the tides within partial-core potentials, with only our most massive SCs ($M_{\rm ini}=4.18\times10^4\,{\rm M}_\odot$) surviving longer than a few Myrs. Such a SC could not be close to the centre of the host potential without experiencing significant tidal disruption, and as discussed above, the chance of observing a high-orbit realization at the projected radius observed in EriII become increasingly unlikely at high radii. Determining a more exact likelihood would require simulations with higher initial orbital radii.

4.3 Could EriII's SC be a luminous sub-halo?

In the end, neither the 'full core' nor 'recent accretion' scenarios are entirely satisfactory. Only the full core scenario is able to support *in situ* SCs of the size seen in EriII. However, such a host potential may be challenging to explain in Λ CDM (see Section 4.1.1). Furthermore, such a large and low-density core is in mild tension with the observed stellar kinematics for EriII (see Fig. 2). By contrast, the 'recent accretion' scenario supports large SCs for our partial core and

weakened cusp models, and naturally reproduces the ellipticity and orientation of the SC in EriII. But, it struggles to consistently support SCs as large as in EriII, and it predicts the formation of denser tidal tails that are absent in observations (Simon et al. 2021).

However, it is interesting to note that the observed properties of the SC in EriII ($M_v = -3.6 \pm 0.6$ mag; Crnojević et al. 2016, $R_{\rm half} = 23 \pm 3 \,\mathrm{pc}$; Simon et al. 2021) place it in an uncertain regime between Milky Way globular clusters and potential dwarf galaxy candidates (see e.g. Fig. 2. of Simon 2019). Therefore, perhaps the SC in EriII is not a true SC, but rather a luminous sub-halo (or the nucleus of a luminous sub-halo) - the remnant of a dwarf galaxy merger. In this scenario, the sub-halo's stellar distribution is shielded from the gravitational tides of EriII by its surrounding dark matter, similar to the behaviour of SCs in dark matter mini-haloes (Boldrini & Vitral 2021; Vitral & Boldrini 2021). This could explain the lack of visible tidal tails, the comparatively large half-light radius and the high ellipticity, as the latter two are more natural properties of dwarf galaxies (Martin, de Jong & Rix 2008; Sanders & Evans 2017; Higgs et al. 2021). Under this scenario, there are looser restrictions on both the infall time and slope of the host potential profile in EriII, so long as the dark matter envelope can effectively shield its stellar content.

With the simplistic assumption that haloes of mass $M_{200} < 10^9 \, \rm M_{\odot}$ are well-fit by extrapolating stellar-to-halo mass relation (e.g. Moster, Naab & White 2013; Read et al. 2017b), a galaxy of $M_* = 4.3 \times 10^3 \, \rm M_{\odot}$ would be hosted by a halo of approximately $M_{200} \sim 5.3 \times 10^8 \, \rm M_{\odot}$. Stars in a dispersion-supported dwarf galaxy inherit that velocity dispersion. Assuming that the velocity anisotropy has minimal impact within a small radius, the mass within the half-light radius can be estimated using the following formula (Wolf et al. 2010):

$$M_{1/2} = 3G \left\langle \sigma_{\rm los}^2 \right\rangle R_{1/2},\tag{6}$$

where σ_{los} is the line-of-sight velocity dispersion. This can be rearranged to give the velocity dispersion based on the half-light radius and corresponding enclosed mass. Assuming EriII's SC (with half-light radius of 15 pc; Simon et al. 2021) inhabits a dark matter sub-halo with an NFW density profile, with a concentration at the median of the expected distribution in Λ CDM (Moliné et al. 2017), this yields $\sigma_{los} \sim 4.2 \, \mathrm{km \, s^{-1}}$. This is consistent with the constraints from the MUSE-Faint survey of $\sigma_{los} < 7.6 \, \mathrm{km \, s^{-1}}$ (Zoutendijk et al. 2020). The dispersion is larger, however, than would be expected for a dark matter-free SC ($\sigma_{los} < 1.5 \, \mathrm{km \, s^{-1}}$; e.g. Contenta et al. 2018) and so this scenario could be tested in future with more radial velocities for SC member stars.

Low-mass luminous sub-haloes with properties comparable to the SC in EriII are present within the EDGE simulation suite (Taylor et al, in prep). However, there are no examples of such sub-haloes which survive infall on to the EDGE galaxies presented here, perhaps due to a need to go to even higher resolution. We will explore such ideas in future work.

5 CONCLUSIONS

We have used a large suite of 960 direct *N*-body simulations of SCs orbiting within spherically symmetric profiles fit to UFD galaxies, simulated as part of the 'Engineering Dwarfs at Galaxy Formation's Edge' (EDGE) project, to model the survival, evolution and properties of EriII's lone SC. We focused, for the first time, on the puzzlingly large ellipticity $(0.31^{+0.05}_{-0.06};$ Simon et al. 2021) of EriII's SC, asking the question: *Can we form a SC as large, offset and elliptical as that in EriII within realistic UFDs in \LambdaCDM?*

As found in prior work, the large size and offset of EriII's SC are naturally explained if it orbits within a central dark matter core of size $\sim 70 \,\mathrm{pc}$ and density $\lesssim 2 \times 10^8 \,\mathrm{M_\odot \,kpc^{-3}}$. Such a flat dark matter core does not form naturally in the EDGE simulations and requires, therefore, either rarer assembly histories than explored in EDGE, additional physics currently missing from EDGE, or a shift to alternative dark matter models (see the discussion in Section 4.1.1). Furthermore, due to the absence of tidal forces within the core, the cored model cannot explain the high ellipticity of EriII's SC through tidal stripping/deformation. However, this same lack of tidal forces causes any primordial birth ellipticity to become 'frozen in' for long periods of time (see Section 3.2.3 and Fig. 7). A high ellipticity may also be found if the SC orbit is observed close to edge-on (see Appendix B), though we find that this is unlikely to explain the ellipticity of the SC in EriII. As such, in the 'full core' model, the ellipticity of EriII's SC must reflect its birth ellipticity, which would be consistent with that of young SCs (Getman et al. 2018).

We also considered whether EriII's SC can be explained if it fell in recently and is currently on the verge of tidal disruption. This requires a central dark matter density for EriII that is not too-cusped and not-too-cored, exactly as predicted for late forming UFDs in the EDGE project (see discussion in Section 4.2). A recent infall may be expected given that our EDGE simulations most similar to EriII assembled late from star-rich minor mergers. If the SC is observed during tidal disruption, then the orientation and ellipticity of EriII's SC are naturally reproduced. However, the primary problems with this model are that it struggles to explain the large size of EriII's SC and, in order to generate an ellipticity as high as that reported for EriII's SC, it produces more significant tidal tails that should have already been detected in current data (see Section 4.2). Such a model requires fine-tuning of the orbit, history and current orientation of EriII's SC.

A mixture of these scenarios may also provide possible solutions for the SC in EriII, but we stress that the presence of a core (or at least a partial-core) is a required feature in all models. Therefore, we currently favour the cored model. However, the 'recent accretion' model could be salvaged if EriII's star cluster is actually a luminous dwarf galaxy and, therefore, tidally protected by a surrounding dark matter halo (see Section 4.3). We will consider this idea in more detail in future work.

At present, the model that comes closest to explaining all the data for EriII's SC requires it to orbit in a large and low-density dark matter core. Such a core is not expected in pure dark matter structure formation simulations in Λ CDM, though it could possibly be explained by baryonic effects (see the discussion in Section 4.1.1). If baryonic effects cannot explain such a core, EriII's puzzling SC may call for us to move beyond the Cold Dark Matter model.

ACKNOWLEDGEMENTS

MO acknowledges the UKRI Science and Technology Facilities Council (STFC) for support (grant ST/R505134/1). This work was performed using the DIRAC Data Intensive service at Leicester, operated by the University of Leicester IT Services, which forms part of the STFC DiRAC HPC Facility (www.dirac.ac.uk). The equipment was funded by BEIS capital funding via STFC capital grants ST/K000373/1 and ST/R002363/1 and STFC DIRAC Operations grant ST/R001014/1. DIRAC is part of the National e-Infrastructure. OA acknowledges support from the Knut and Alice Wallenberg Foundation and the Swedish Research Council (grant 2019-04659). This project has received funding from the European Union's Horizon 2020 research and innovation programme under

grant agreement No. 818085 GMGalaxies. AP was supported by the Royal Society. MR is supported by the Beecroft Fellowship funded by Adrian Beecroft and the Knut and Alice Wallenberg Foundation. ET acknowledges the UKRI Science and Technology Facilities Council (STFC) for support (grant ST/V50712X/1). MD acknowledges support by ERC-Syg 810218 WHOLE SUN. We acknowledge Prof. Josh Simon for his helpful guidance, Prof. Mark Gieles for his useful advice on globular cluster evolution, Sebastiaan Zoutendijk for sharing his constraints on the density profile of Eridanus II, and the anonymous reviewer for their valuable comments.

In addition to software already mentioned, this work has made use of the public software PYTHON (Van Rossum & Drake 2009), NUMPY (Van der Walt, Colbert & Varoquaux 2011), SCIPY (Virtanen et al. 2020) and MATPLOTLIB (Hunter 2007).

AUTHOR CONTRIBUTIONS

The main roles of the authors were, using the CRediT (Contribution Roles Taxonomy) system⁶:

MO: Conceptualization; Data curation; Formal analysis; Investigation (lead); Writing – original draft. JR: Conceptualization; Funding Acquisition; Project Administration; Resources; Writing – review and editing OA: Funding Acquisition; Methodology; Software; Writing – review and editing. AP: Conceptualization; Funding Acquisition; Methodology; Writing – review and editing. MR: Conceptualization; Data curation; Methodology; Writing – review and editing. AG: Methodology. ET: Conceptualization. SK: Conceptualization. MD: Software.

DATA AVAILABILITY

Data available upon reasonable request.

REFERENCES

Aarseth S. J., 1999, Publ. Astron. Soc. Pac., 111, 1333

Aarseth S. J., Binney J., 1978, MNRAS, 185, 227

Agekian T. A., 1958, Soviet Astron., 2, 22

Agertz O., Kravtsov A. V., Leitner S. N., Gnedin N. Y., 2013, ApJ, 770, 25 Agertz O. et al., 2020, MNRAS, 491, 1656

Allison R. J., Goodwin S. P., Parker R. J., de Grijs R., Portegies Zwart S. F., Kouwenhoven M. B. N., 2009, ApJ, 700, L99

Amorisco N. C., 2017, ApJ, 844, 64

Balbinot E., Gieles M., 2018, MNRAS, 474, 2479

Banik U., van den Bosch F. C., 2021, ApJ, 912, 43

Banik N., Bovy J., Bertone G., Erkal D., de Boer T. J. L., 2021, J. Cosmol. Astropart. Phys., 2021, 043

Baumgardt H., Makino J., 2003, MNRAS, 340, 227

Bechtol K. et al., 2015, ApJ, 807, 50

Bianchini P., Varri A. L., Bertin G., Zocchi A., 2013, ApJ, 772, 67

Bianchini P., van der Marel R. P., del Pino A., Watkins L. L., Bellini A., Fardal M. A., Libralato M., Sills A., 2018, MNRAS, 481, 2125

Boldrini P., Vitral E., 2021, MNRAS, 507, 1814

Bolte M., 1989, ApJ, 341, 168

Bonnell I. A., Davies M. B., 1998, MNRAS, 295, 691

Bouché N. F. et al., 2022, A&A, 658, A76

Boylan-Kolchin M., Bullock J. S., Kaplinghat M., 2011, MNRAS, 415, L40

Carignan C., Freeman K. C., 1988, ApJ, 332, L33

Chabrier G., 2003, PASP, 115, 763

 $^6 \rm https://authorservices.wiley.com/author-resources/Journal-Authors/open-access/credit.html$

Chan T. K., Kereš D., Oñorbe J., Hopkins P. F., Muratov A. L., Faucher-Giguère C. A., Quataert E., 2015, MNRAS, 454, 2981

Chandrasekhar S., 1943, ApJ, 97, 255

Clowe D., Bradač M., Gonzalez A. H., Markevitch M., Randall S. W., Jones C., Zaritsky D., 2006, ApJ, 648, L109

Cole D. R., Dehnen W., Read J. I., Wilkinson M. I., 2012, MNRAS, 426, 601 Contenta F. et al., 2018, MNRAS, 476, 3124

Correa C. A., 2021, MNRAS, 503, 920

Crnojević D., Sand D. J., Zaritsky D., Spekkens K., Willman B., Hargis J. R., 2016, ApJ, 824, L14

Dawson K. S. et al., 2013, AJ, 145, 10

Dehnen W., 1993, MNRAS, 265, 250

Dhoke P., Paranjape A., 2021, MNRAS, 508, 852

Di Cintio A., Brook C. B., Macciò A. V., Stinson G. S., Knebe A., Dutton A. A., Wadsley J., 2014, MNRAS, 437, 415

Diemand J., Moore B., Stadel J., 2005, Nature, 433, 389

Diemand J., Kuhlen M., Madau P., 2007, ApJ, 667, 859

Diemer B., More S., Kravtsov A. V., 2013, ApJ, 766, 25

Dutton A. A., Macciò A. V., 2014, MNRAS, 441, 3359

Eggleton P. P., Fitchett M. J., Tout C. A., 1989, ApJ, 347, 998

Einsel C., Spurzem R., 1999a, MNRAS, 302, 81

Einsel C., Spurzem R., 1999b, MNRAS, 302, 81

Elahi P. J., Mahdi H. S., Power C., Lewis G. F., 2014, MNRAS, 444, 2333

Enzi W. et al., 2021, MNRAS, 506, 5848

Fall S. M., Frenk C. S., 1983, AJ, 88, 1626

Ferraro F. R. et al., 2018, ApJ, 860, 50

Fitts A. et al., 2019, MNRAS, 490, 962

Flores R. A., Primack J. R., 1994, ApJ, 427, L1

Foreman-Mackey D., Hogg D. W., Lang D., Goodman J., 2013, PASP, 125, 306

Garrison-Kimmel S., Rocha M., Boylan-Kolchin M., Bullock J. S., Lally J., 2013, MNRAS, 433, 3539

Genzel R. et al., 2020, ApJ, 902, 98

Getman K. V., Kuhn M. A., Feigelson E. D., Broos P. S., Bate M. R., Garmire G. P., 2018, MNRAS, 477, 298

Gnedin O. Y., Hernquist L., Ostriker J. P., 1999, ApJ, 514, 109

Goerdt T., Moore B., Read J. I., Stadel J., Zemp M., 2006, MNRAS, 368,

Goerdt T., Moore B., Read J. I., Stadel J., 2010, ApJ, 725, 1707

Goodwin S. P., 1997, MNRAS, 286, L39

Gutcke T. A., Pakmor R., Naab T., Springel V., 2022, MNRAS, 513, 1372

Haardt F., Madau P., 1996, ApJ, 461, 20

Harris W. E., 2010, preprint (arXiv:1012.3224)

Higgs C. R., McConnachie A. W., Annau N., Irwin M., Battaglia G., Côté P., Lewis G. F., Venn K., 2021, MNRAS, 503, 176

Hofmann S., Schwarz D. J., Stöcker H., 2001, Phys. Rev. D, 64, 083507

Hunter J. D., 2007, Comput. Sci. Eng., 9, 90

Hurley J. R., 2008, in Aarseth S. J., Tout C. A., Mardling R. A., eds, Lecture Notes in Physics, Vol. 760, The Cambridge N-Body Lectures. Springer-Verlag, Berlin, p.283

Hurley J. R., Pols O. R., Tout C. A., 2000, MNRAS, 315, 543

Hurley J. R., Tout C. A., Pols O. R., 2002, MNRAS, 329, 897

Kamann S. et al., 2018, MNRAS, 473, 5591

Kaur K., Sridhar S., 2018, ApJ, 868, 134

Kimm T., Cen R., Devriendt J., Dubois Y., Slyz A., 2015, MNRAS, 451, 2900
Klimentowski J., Łokas E. L., Kazantzidis S., Mayer L., Mamon G. A., Prada F., 2009, MNRAS, 400, 2162

Klypin A., Kravtsov A. V., Valenzuela O., Prada F., 1999, ApJ, 522, 82Koposov S. E., Belokurov V., Torrealba G., Evans N. W., 2015, ApJ, 805, 130

Kroupa P., 2002, Science, 295, 82

Kundic T., Ostriker J. P., 1995, ApJ, 438, 702

Küpper A. H. W., Kroupa P., Baumgardt H., Heggie D. C., 2010, MNRAS, 401, 105

Küpper A. H. W., Maschberger T., Kroupa P., Baumgardt H., 2011, MNRAS, 417, 2300

Li T. S. et al., 2017, ApJ, 838, 8

Lin H. W., Loeb A., 2016, J. Cosmology Astropart. Phys., 2016, 009

Longaretti P.-Y., Lagoute C., 1996, A&A, 308, 453

Lovell M. R., Hellwing W., Ludlow A., Zavala J., Robertson A., Fattahi A., Frenk C. S., Hardwick J., 2020, MNRAS, 498, 702

Ludlow A. D., Navarro J. F., Angulo R. E., Boylan-Kolchin M., Springel V., Frenk C., White S. D. M., 2014, MNRAS, 441, 378

Lynden-Bell D., 1967, MNRAS, 136, 101

Macciò A. V., Paduroiu S., Anderhalden D., Schneider A., Moore B., 2012, MNRAS, 424, 1105

Mackey A. D., Da Costa G. S., Ferguson A. M. N., Yong D., 2013, ApJ, 762,

Malhan K., Valluri M., Freese K., 2021, MNRAS, 501, 179

Martin N. F., de Jong J. T. A., Rix H.-W., 2008, ApJ, 684, 1075

Martin N. F. et al., 2016, ApJ, 833, 167

Martínez-Vázquez C. E. et al., 2021, MNRAS, 508, 1064

Mashchenko S., Sills A., 2005a, ApJ, 619, 243

Mashchenko S., Sills A., 2005b, ApJ, 619, 258

Mashchenko S., Couchman H. M. P., Wadsley J., 2006, Nature, 442, 539

Mashchenko S., Wadsley J., Couchman H. M. P., 2008, Science, 319, 174

Maxwell A. J., Wadsley J., Couchman H. M. P., 2015, ApJ, 806, 229

McGaugh S. S., Rubin V. C., de Blok W. J. G., 2001, AJ, 122, 2381

Moliné Á., Sánchez-Conde M. A., Palomares-Ruiz S., Prada F., 2017, MNRAS, 466, 4974

Moore B., 1994, Nature, 370, 629

Moore B., Ghigna S., Governato F., Lake G., Quinn T., Stadel J., Tozzi P., 1999, ApJ, 524, L19

Moster B. P., Naab T., White S. D. M., 2013, MNRAS, 428, 3121

Nadler E. O., Birrer S., Gilman D., Wechsler R. H., Du X., Benson A., Nierenberg A. M., Treu T., 2021, ApJ, 917, 7

Navarro J. F., Eke V. R., Frenk C. S., 1996a, MNRAS, 283, L72

Navarro J. F., Frenk C. S., White S. D. M., 1996b, ApJ, 462, 563

Navarro J. F., Frenk C. S., White S. D. M., 1997, ApJ, 490, 493

Newville M., Stensitzki T., Allen D. B., Rawlik M., Ingargiola A., Nelson A., 2016, Astrophysics Source Code Library, record ascl:1606.014

Nitadori K., Aarseth S. J., 2012, MNRAS, 424, 545

Oka A., Saito S., Nishimichi T., Taruya A., Yamamoto K., 2014, MNRAS, 439, 2515

Okamoto T., Frenk C. S., 2009, MNRAS, 399, L174

Oñorbe J., Boylan-Kolchin M., Bullock J. S., Hopkins P. F., Kereš D., Faucher-Giguère C.-A., Quataert E., Murray N., 2015, MNRAS, 454, 2092

Orkney M. D. A., Read J. I., Petts J. A., Gieles M., 2019, MNRAS, 488, 2977 Orkney M. D. A. et al., 2021, MNRAS, 504, 3509

Peñarrubia J., Pontzen A., Walker M. G., Koposov S. E., 2012, ApJ, 759, L42 Petts J. A., Gualandris A., Read J. I., 2015, MNRAS, 454, 3778

Petts J. A., Read J. I., Gualandris A., 2016, MNRAS, 463, 858

Planck Collaboration XVI, 2014, A&A, 571, A16

Plummer H. C., 1911, MNRAS, 71, 460

Pontzen A., Governato F., 2012, MNRAS, 421, 3464

Pontzen A., Tremmel M., 2018, ApJS, 237, 23

Pontzen A., Roškar R., Stinson G. S., Woods R., Reed D. M., Coles J., Quinn T. R., 2013, Astrophysics Source Code Library, record ascl:1305.002

Pontzen A., Rey M. P., Cadiou C., Agertz O., Teyssier R., Read J., Orkney M. D. A., 2021, MNRAS, 501, 1755

Power C., Navarro J. F., Jenkins A., Frenk C. S., White S. D. M., Springel V., Stadel J., Quinn T., 2003, MNRAS, 338, 14

Prgomet M., Rey M. P., Andersson E. P., Segovia Otero A., Agertz O., Renaud F., Pontzen A., Read J. I., 2022, MNRAS, 513, 2326

Read J. I., Gilmore G., 2005, MNRAS, 356, 107

Read J. I., Steger P., 2017, MNRAS, 471, 4541

Read J. I., Wilkinson M. I., Evans N. W., Gilmore G., Kleyna J. T., 2006a, MNRAS, 366, 429

Read J. I., Goerdt T., Moore B., Pontzen A. P., Stadel J., Lake G., 2006b, MNRAS, 373, 1451

Read J. I., Agertz O., Collins M. L. M., 2016, MNRAS, 459, 2573

Read J. I., Iorio G., Agertz O., Fraternali F., 2017a, MNRAS, 467, 2019

Read J. I., Iorio G., Agertz O., Fraternali F., 2017b, MNRAS, 467, 2019

Read J. I., Walker M. G., Steger P., 2018, MNRAS, 481, 860

Read J. I., Walker M. G., Steger P., 2019, MNRAS, 484, 1401

Reed B. C., 1998, J. R. Astron. Soc., 92, 36

Renaud F., Gieles M., Boily C. M., 2011, MNRAS, 418, 759

Rey M. P., Pontzen A., 2018, MNRAS, 474, 45

Rey M. P., Pontzen A., Agertz O., Orkney M. D. A., Read J. I., Saintonge A., Pedersen C., 2019, ApJ, 886, L3

Rey M. P., Pontzen A., Agertz O., Orkney M. D. A., Read J. I., Rosdahl J., 2020, MNRAS, 497, 1508

Rey M. P., Pontzen A., Agertz O., Orkney M. D. A., Read J. I., Saintonge A., Kim S. Y., Das P., 2022, MNRAS, 511, 5672

Richardson T., Fairbairn M., 2014, MNRAS, 441, 1584

Roth N., Pontzen A., Peiris H. V., 2016, MNRAS, 455, 974

Sand D. J., Treu T., Ellis R. S., 2002, ApJ, 574, L129

Sanders J. L., Evans N. W., 2017, MNRAS, 472, 2670

Sanders J. L., Evans N. W., Dehnen W., 2018, MNRAS, 478, 3879

Schmidt M., 1959, ApJ, 129, 243

Schneider A., Smith R. E., Macciò A. V., Moore B., 2012, MNRAS, 424, 684 Shao S., Cautun M., Frenk C. S., Reina-Campos M., Deason A. J., Crain R. A., Kruijssen J. M. D., Pfeffer J., 2021, MNRAS, 507, 2339

Shapiro S. L., Marchant A. B., 1976, ApJ, 210, 757

Sharma G., Salucci P., van de Ven G., 2022, A&A, 659, A40

Shi Y., Zhang Z.-Y., Wang J., Chen J., Gu Q., Yu X., Li S., 2021, ApJ, 909, 20

Simon J. D., 2019, ARA&A, 57, 375

Simon J. D. et al., 2021, ApJ, 908, 18

Springel V., Frenk C. S., White S. D. M., 2006, Nature, 440, 1137

Stopyra S., Pontzen A., Peiris H., Roth N., Rey M. P., 2021, ApJS, 252, 28

Strigari L. E., Frenk C. S., White S. D. M., 2017, ApJ, 838, 123

Susa H., Umemura M., 2004, ApJ, 600, 1

Tegmark M. et al., 2006, Phys. Rev. D, 74, 123507

Teyssier R., 2002, A&A, 385, 337

Tiongco M. A., Vesperini E., Varri A. L., 2017, MNRAS, 469, 683

Tollet E. et al., 2016, MNRAS, 456, 3542

Tout C. A., Aarseth S. J., Pols O. R., Eggleton P. P., 1997, MNRAS, 291, 732 Trujillo-Gomez S., Kruijssen J. M. D., Keller B. W., Reina-Campos M., 2021, MNRAS, 506, 4841

Van der Walt S., Colbert S. C., Varoquaux G., 2011, Comput. Sci. Eng., 13, 22

Van Rossum G., Drake F. L., 2009, Python 3 Reference Manual. CreateSpace, Scotts Valley, CA

Virtanen P. et al., 2020, Nat. Methods, 17, 261

Vitral E., Boldrini P., 2021, MNRAS, preprint (arXiv:2112.01265)

Vogelsberger M., Zavala J., Loeb A., 2012, MNRAS, 423, 3740

Wang W., White S. D. M., Mandelbaum R., Henriques B., Anderson M. E., Han J., 2016, MNRAS, 456, 2301

Wang K., Mao Y.-Y., Zentner A. R., Lange J. U., van den Bosch F. C., Wechsler R. H., 2020a, MNRAS, 498, 4450

Wang J., Bose S., Frenk C. S., Gao L., Jenkins A., Springel V., White S. D. M., 2020b, Nature, 585, 39

Webb J. J., Reina-Campos M., Kruijssen J. M. D., 2019, MNRAS, 486, 5879Wechsler R. H., Bullock J. S., Primack J. R., Kravtsov A. V., Dekel A., 2002,ApJ, 568, 52

Weinberg M. D., 1994, AJ, 108, 1403

Wheeler C. et al., 2019a, MNRAS, 490, 4447

Wheeler C. et al., 2019b, MNRAS, 490, 4447

Wolf J., Martinez G. D., Bullock J. S., Kaplinghat M., Geha M., Muñoz R. R., Simon J. D., Avedo F. F., 2010, MNRAS, 406, 1220

Zoutendijk S. L. et al., 2020, A&A, 635, A107

Zoutendijk S. L. et al., 2021a, A&A, preprint (arXiv:2112.09374)

Zoutendijk S. L., Brinchmann J., Bouché N. F., den Brok M., Krajnović D., Kuijken K., Maseda M. V., Schaye J., 2021b, A&A, 651, A80

APPENDIX A: SHAPE FIT WITH DIFFERENT METHODS

Throughout this paper, we estimate the shapes of SCs using the analysis.halo.halo.shape() function in PYNBODY (modified for 2D distributions), which iteratively solves the moment of inertia tensor. If the SC shape varies as a function of radius, as is

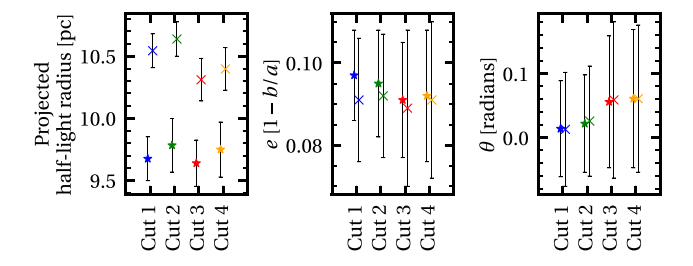


Figure A1. Comparison of the projected half-light radius, ellipticity and orientation angle for a single example SC using different methods and luminosity cuts. Stars represent results using the direct analytical methods (direct calculation of the projected half-light radius and an iterative fit for the shape properties), whereas crosses represent results yielded by an MCMC method. The luminosity cuts are: **Cut 1** (blue): $0.1 \ge L_V/L_{\odot, V} \ge 20$, **Cut 2** (green): $0.1 \ge L_V/L_{\odot, V} \ge 100$, **Cut 3** (red): $0.5 \ge L_V/L_{\odot, V} \ge 20$, **Cut 4** (gold): $0.5 \ge L_V/L_{\odot, V} \ge 100$. Error bars represent the one-sigma uncertainties

the case for many of the simulations presented here, then the results depend on the size of the region that is fitted to. In our calculations, the definition of this region involves the half-light radius of the SC. This half-light calculation may itself be sensitive to the chosen luminosity cuts of the SC stars.

The size and shape of observed stellar distributions are typically estimated using fits like in Martin et al. (2008), Martin et al. (2016). To confirm that our numerical properties are analogous to such methods, we compare using a method developed by Goater et al (in prep). This method is based upon the affine-invariant Markov Chain Monte Carlo (MCMC) ensemble sampler EMCEE (Foreman-Mackey et al. 2013), and assumes a surface brightness profile which is fit to the simulated stellar data. Once appropriately normalized, it represents the mass-weighted probability of finding a star, i, at a given position, r_i , as,

$$l_i = \frac{882N}{625\pi R_{1/2}^2 (1 - \epsilon)} \exp\left(\frac{-42r_i}{25R_{1/2}}\right) \frac{m_i}{M},\tag{A1}$$

where N is the number of stars in the sample, M is the total stellar mass, m_i the individual stellar mass, ϵ is the ellipticity defined as $\epsilon = 1 - b/a$, with b/a as the minor-to-major-axial ratio of the system, θ is the position angle of the major axis, and $R_{1/2}$ is the projected half-light radius of the exponential radial profile. The elliptical radius is related to the stellar positions as:

$$r_i = \left[\left(\frac{1}{1 - \epsilon} (x_i \cos \theta - y_i \sin \theta) \right)^2 + (x_i \sin \theta + y_i \cos \theta)^2 \right]^{\frac{1}{2}}.$$
(A2)

The total likelihood is the product of all probabilities, which is then calculated as:

$$\ln \mathcal{L} = \sum_{i} \ln l_i.$$
(A3)

We place flat priors for ϵ , θ , and $R_{1/2}$ such that the $0 \le \epsilon < 1$, $-\pi \le \theta \le \pi$, and $R_{1/2} > 0$. When fitting SCs we use the additional constraint that $R_{1/2} \le 2 \times R_{1/2,numerical}$, where $R_{1/2,numerical}$ is the numerically calculated projected half-light radius. Whilst this function is technically fit to the stellar mass distribution rather than the light distribution, it is often assumed that observed systems have uniform stellar populations unaffected by mass segregation (Martin et al. 2016). This approximation may be dubious for globular cluster systems (see Bolte 1989; Bonnell & Davies 1998; Allison et al. 2009).

In Fig. A1, we compare the size and shape for a single example, SC as calculated using different methods and luminosity cuts. When using the MCMC method, we use 100 walkers with 500 burn-in steps and 2000 main steps. The one-sigma uncertainties are similar between methods and luminosity cuts. The estimated ellipticity and orientation are almost identical between methods, however the MCMC method overestimates the projected half-light radius by a few sigma when compared to the direct analytical method. This overestimate can be very large for SCs that are close to dissolving, but is otherwise $\lesssim 1$ pc across our simulation suite. Therefore, whilst the two methods are not formally in agreement, the expected systematic error of $\lesssim 1$ pc does not influence our results. The choice of luminosity cut has a small effect on the size, ellipticity and orientation of the SC, but the magnitude of this effect is within the one-sigma uncertainties.

APPENDIX B: STAR CLUSTER SHAPE FROM AN EDGE-ON PERSPECTIVE

A SC in a cored potential can experience negligible gravitational tides in the face-on plane of its orbit, yet still experience a tidal compression across its *z*-axis (see equation 21, Renaud, Gieles & Boily 2011). Therefore, it is necessary to consider the SC shape from both face-on and edge-on orientations for a complete understanding of the SC ellipticity.

In Fig. B1, we reconsider the SC shapes from Fig. 6, but as viewed edge-on to the orbital plane. Now, there is a sharp spike of SCs at higher ellipticities. This is due in part to a tidal compression across the z-axis, but primarily contamination from tidally stripped stars which form a dense track when viewed edge-on. If we exclude all unbound stars from our analysis, then only seven examples (in models Halo1459 and Halo1459 GM:Later) exceed e = 0.15. The ellipticities of SCs in the Fcore potential remain low in almost all cases, because the flatter potential liberates fewer stars. A single data

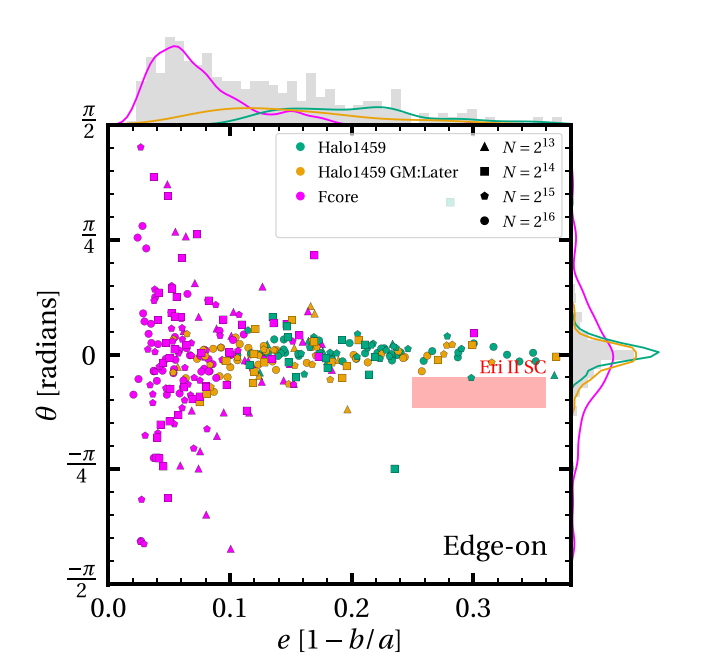


Figure B1. The orientation θ versus ellipticity e for all surviving SC simulations after a Hubble time, as in Fig. 6, but as viewed edge-on to the orbital plane. A combination of tidal debris, which is denser when viewed edge-on to the orbit, and tidal compression leads to a greater ellipticity for many SCs.

point in the Fcore potential achieves an ellipticity comparable to that of the SC in EriII, but it is a near-destroyed SC that does not match EriII in any other respect.

These increased ellipticities are predominantly a consequence of our idealized simulations, where the SC orbit remains in the same x–y plane and the unbound stars remain dynamically cold for a full Hubble time. Even then, the SC must be viewed extremely close to edge-on before the perceived ellipticity increases notably.

APPENDIX C: ENERGY REQUIREMENTS FOR DARK MATTER CORE FORMATION IN THE EDGE UFDS

We perform a simple comparison of the energy required to unbind our dark matter cusps with the available energy provided by SNe explosions, following prior work in Peñarrubia et al. (2012), Read et al. (2016), Contenta et al. (2018), Trujillo-Gomez et al. (2021). We make this comparison at z=4 because star formation has permanently quenched by this time, noting, however, that this does not account for the additional late-time coring due to minor mergers in Halo1459 GM:Later.

We estimate the SNe energy from the IMF as follows:

$$E_{\rm SF} = \frac{M_* \xi E_{\rm SN}}{\langle m_* \rangle},\tag{C1}$$

where M_* is the total stellar mass of the galaxy at z=4, $\langle m_* \rangle$ is the expectation value for the stellar mass, ξ is the number fraction of stars that become SNe $(m_*>8\,\mathrm{M}_\odot)$ and $E_\mathrm{SN}=10^{51}\,\mathrm{erg}$ is the energy per SNe. Our implementation of RAMSES utilizes a Chabrier IMF (Chabrier 2003), for which we evaluate $\langle m_* \rangle$ and ξ by integrating over the range $0.1 < m_*/\mathrm{M}_\odot < 120$ as 0.680 and 0.00802, respectively. This is an imperfect representation of the SNe energy because it does not consider that some SNe could have occurred whilst an accreted stellar particle was still $ex\ situ$, and may not have contributed directly to the dynamical heating of the main progenitor.

Table C1. Comparison of the estimated total SNe energy $(E_{\rm SN})$, the energy required to lower the central density cusp (cusp gravitational binding energy minus core gravitational binding energy, ΔW), and the coupling efficiency $(\epsilon_{\rm DM})$ for the chosen EDGE haloes at z=4. For the calculation of $E_{\rm SN}$, we consider only stars within the core radius (taken from coreNFW profile fits, Read et al. 2016), as stars exterior to this radius do not contribute to the heating of the dark matter cusp.

Name	E _{SN} [erg]	ΔW [erg]	ϵ_{DM}
Halo1445 Halo1459	$7.28 \times 10^{53} \\ 1.17 \times 10^{54}$	$1.10 \times 10^{50} 1.09 \times 10^{50}$	$1.51 \times 10^{-4} 9.37 \times 10^{-5}$
Halo1459 GM:Later	2.72×10^{53}	7.07×10^{49}	2.60×10^{-4}

The energy needed to depress the central density can be found by analysing the enclosed mass profiles of the haloes at z=4. We fit a coreNFW profile (Read et al. 2016) where the concentration parameter c is constrained based on fits from Dutton & Macciò (2014). A cuspy profile is approximated by setting the parameter n=0 (equivalent to an NFW profile Navarro et al. 1997). Then, the energy difference ΔW between the cuspy NFW and fitted coreNFW profiles is calculated as in equation (22) of Read et al. (2016):

$$\Delta W = -\frac{1}{2} \int_0^\infty \frac{G(M_{\text{NFW}}^2 - M_{\text{coreNFW}}^2)}{r^2} \, \mathrm{d}r. \tag{C2}$$

A coupling efficiency between the SNe energy and dark matter is defined as $\Delta W/E_{SF}$. The results are summarized in Table C1.

Although Halo1459 and Halo1459 GM:Later are based upon the same modified initial conditions, Halo1459 GM:Later requires less energy to unbind its dark matter cusp. This is because the later assembly of Halo1459 GM:Later has left it with a diminished central density at the earliest times. Halo1445 exhibits a similar coupling efficiency to Halo1459 GM:Later, which also owes to its delayed mass growth.

This paper has been typeset from a $T_{\!\!E}X/L\!\!\!/\!\!T_{\!\!E}X$ file prepared by the author.